# Predicting cognitive decline in a low-dimensional representation of brain morphology

**Rémi Lamontagne-Caron[1,2,*], Patrick Desrosiers[2,3,4], Olivier Potvin[2], Simon Duchesne[2,5], Nicolas Doyon[2,3,6], the Alzheimer's Disease Neuroimaging Initiative[+], and the CIMA-Q**

[1]Département de médecine, Université Laval, Québec (Québec), Canada, G1V 0A6
[2]Centre de recherche CERVO, Québec (Québec), Canada G1J 2G3
[3]Centre interdisciplinaire en modélisation mathématique, Université Laval, Québec (Québec), Canada, G1V 0A6
[4]Département de physique, de génie physique et d'optique , Université Laval, Québec (Québec), Canada, G1V 0A6
[5]Département de radiologie et médecine nucléaire, Université Laval, Québec (Québec), Canada, G1V 0A6
[6]Département de mathématiques et de statistique, Université Laval, Québec (Québec), Canada, G1V 0A6
[*]remi.lamontagne-caron.1@ulaval.ca
[+]Data used in preparation of this article were obtained from the Alzheimer's Disease Neuroimaging Initiative (ADNI) database (adni.loni.usc.edu). As such, the investigators within the ADNI contributed to the design and implementation of ADNI and/or provided data but did not participate in analysis or writing of this report. A complete listing of ADNI investigators can be found at this link.

## ABSTRACT

Identifying early signs of neurodegeneration due to Alzheimer's disease (AD) is a necessary first step towards preventing cognitive decline. Individual cortical thickness measures, available after processing anatomical magnetic resonance imaging (MRI), are sensitive markers of neurodegeneration. However, normal aging cortical decline and high inter-individual variability complicate the comparison and statistical determination of the impact of AD-related neurodegeneration on trajectories. In this paper, we computed trajectories of thickness changes in a 2D representation of a 62-dimensional manifold of individual cortical thickness measures. To compute this representation, we used a novel, nonlinear dimension reduction algorithm called Uniform Manifold Approximation and Projection (UMAP). We first trained a UMAP embedding on cortical thickness measurements of 6,237 cognitively healthy participants (3,556 women) aged 18 to 100 years old. Once transformed and rotated, its principal axis was shown to be positively associated ($r = 0.65$) with participants' age. We then projected in this transformed UMAP space, data from longitudinal MRIs of 537 mild cognitively impaired (MCI) subjects and 340 AD subjects from the Alzheimer's Disease Neuroimaging Initiative database. Each participant had multiple visits ($n \geq 2$), one year apart. Once in the transformed UMAP space, the data was clustered using a $k$-means variant. Average trajectories between clusters were shown to be significantly different between MCI and AD subjects. Moreover, we showed that some clusters and trajectories between clusters were more prone to host AD subjects. This study was able to differentiate AD and MCI subjects based on their cluster trajectory in a 2D space with a AUC of 0.72 over 2,000 iterations.

## Introduction

A proper understanding of brain morphology trajectory during cognitively healthy aging can be leveraged to detect departures due to neurodegeneration (e.g. from Alzheimer's disease (AD)) and therefore serve as an early indicator of incipient dementia. As the socio-economical costs of AD increase with the aging of global populations[1,2], early detection becomes the only approach which allows for the possibility of interventions able to reduce the risk of conversion to dementia.

Brain morphology can be assessed via magnetic resonance imaging (MRI)[3–6]. Morphometry has been shown to be a sensitive marker of neurodegeneration[7,8]. However, normal aging cortical decline and high inter-individual variability complicate the comparison and statistical determination of the impact of AD-related neurodegeneration on trajectories. Further, the high-dimensional nature of morphometry (whereas the available measurements routinely surpass the number of study participants) necessitate the use of a transformation into lower-dimensional spaces in order to perform statistical analyses, modelling or machine learning[9–12]. In these resulting spaces of low dimensionality, the task then turns to the identification of criteria with which to determine whether a given brain morphology trajectory is pathological or not, which implies having comparative instances of both successful and pathological natures.

High-to-low dimensionality transformations have been carried out via a number of approaches in the past. In some instances, dimensionality reduction or machine learning algorithms were applied directly to the raw voxel data[13–16]. Other approaches first use tools (e.g. FreeSurfer[17]) to extract features such as volumes, thicknesses or surface areas for individual brain structure, then perform dimensionality reduction on the feature vectors[18–22]. While the first family of approaches may yield classifiers with adequate accuracy, the lower-dimensional space and resulting classification functions are usually difficult to interpret. On the other hand, the second family of approaches allows the association between principal dimensions to interpretable features with biological meaning[23], which in turn might suggest intervention strategies.

There remains a question as to whether linear or nonlinear dimensionality reduction techniques should be utilized. In our context, studies of brain morphology in aging have concluded that whole brain volume trajectories as well as microstructural and focal markers exhibit nonlinear patterns[24,25]. More recently, we have shown that atrophy across the brain follows for the most part a quadratic trajectory[26]. Thus, in order for any lower-dimensional embedding to correctly encompass this multi-dimensional problem, a nonlinear dimension reduction algorithm has to be used.

In that class, Uniform Manifold Approximation and Projection (UMAP) is a novel entry, first published in 2018.[27] UMAP's backbone rests on Riemannian manifold theory and topological data analysis. Its main advantage over other nonlinear methods, like t-distributed Stochastic Neighbor Embedding (t-SNE)[28] or nonlinear principal component analysis[29], comes from its agility, performance and conservation of global structures. Further, as opposed to highly nonlinear deep learning networks, a UMAP based method is interpretable through visualization. It is therefore a suitable technique to handle the nonlinear nature of brain morphological trajectories and embed our data vectors in a lower-dimensional space. Examples of similar applications can be found in Campbell et al. and Becht et al.[30,31]

In this article, we present our work on brain morphology trajectory estimation in aging on a number of well-known, publicly available datasets composed of individuals across the spectrum of cognitive health. In a first step, we used UMAP to generate a low-dimensional representation of morphology from vectors of features describing the thicknesses of different brain regions ; in our second step, we used a linear transformation over the UMAP embedding to further highlight the age dependency of the data. In this space, we then identified aging trajectories and were able to compare and predict the future course of individuals that remained either cognitively impaired (MCI), that is in a prodromal state of AD, or declined to clinically probable AD. We then tried different discretization schemes to achieve the best possible accuracy at predicting the longitudinal cognitive outcome in individuals according to their trajectories in the transformed UMAP space.

## Methods

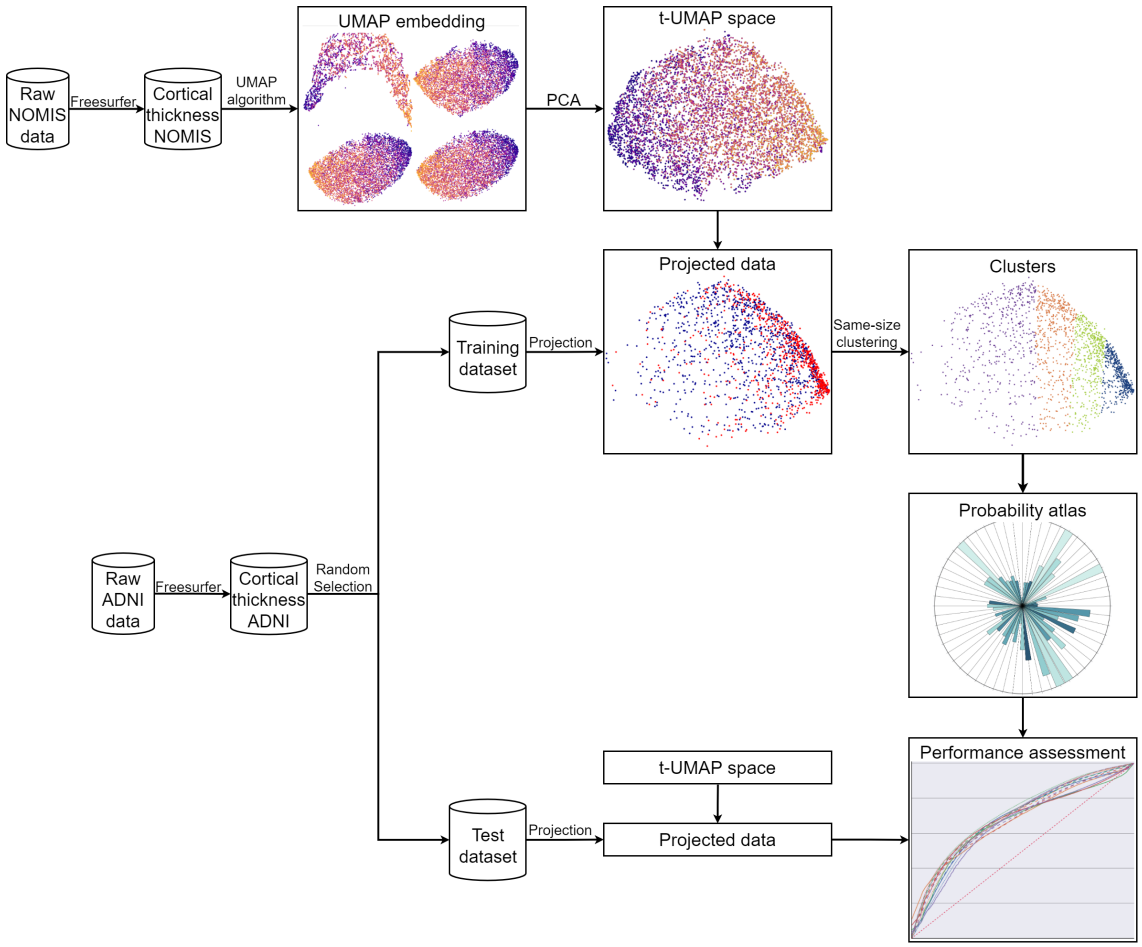


**Figure 1.** Methodological pipeline for the prediction of cognitive outcome. We first generate a low-dimensional representation of morphology from vectors of features describing the thicknesses of different brain regions using UMAP. Next, we linearly transform the UMAP embedding. In this space, we cluster data using a modified k-means algorithm. This allows us to track aging vs. AD progression trajectories between clusters and therefore compare and predict the future course of individuals that remained either cognitively impaired (MCI), that is in a prodromal state of AD, or declined to clinically probable AD.

### Ethics

Approval for the study was obtained from the Ethics review committee of the CERVO Brain Research Center (NSM-2021-2022). Approval from local ethics board and informed consent for all participants were obtained for all datasets in this study (see 1).

### Participants

#### *NOMIS*

The NOMIS database[26] was used to train UMAP's dimensionality reduction model. The database is composed of a total of 6,237 CH participants (3,556 women), aged 18 to 100 years old (median 56 y.o.), and aggregated from 26 different databases[26]. Participants had no history of mental disorder the likes of schizophrenia or other psychotic disorders, bipolar disorders, major depressive disorders (recurrent), post-traumatic stress disorder, substance abuse/dependence disorders, neurodegenerative and neurological disorders, head injury with loss of consciousness/amnesia, lead poisoning or geriatric depression. Since those participants were scanned once, the NOMIS data is cross-sectional.

#### *ADNI*

The Alzheimer's Disease Neuroimaging Initiative (ADNI) database (ADNI1, GO, 2 and 3)[32] was used to test the UMAP model for the prediction of cognitive decline. Launched in 2003 as a public-private partnership, led by Principal Investigator Michael W. Weiner, MD, ADNI's goal has been to test whether serial MRI, positron emission tomography, other biological

markers, and clinical and neuropsychological assessment can be combined to measure the progression of MCI and early AD. For up-to-date information, see www.adni-info.org. All ADNI participants with longitudinal time points and at least one follow-up after the baseline scan were selected for this project, for a total of 1354 participants (604 women). We used ADNI's clinical diagnostic categorization at baseline (526 CH; 828 MCI; 0 AD) and last available follow-up (477 CH, 537 MCI; 340 AD), see Supplementary Table S3 to S5 for more details.

#### *Diagnostic criteria*

For the first ADNI cohort, the criteria for classification between CH, MCI and AD were based on memory loss, the Mini-Mental State Examination (MMSE), the Clinical Dementia Rating score and one paragraph from the Logical Memory II subscale of the Wechsler Memory Scale–Revised. For memory loss, participants needed to have complained about lapses in their memory to be classified as MCI or AD, while CH subjects did not experience memory lapses. With the MMSE, CH and MCI subjects had to have a score between 24 and 30, and for AD, 20-26. Cognitively healthy participants had to have a Clinical Dementia Rating score of 0, MCI 0.5 with the memory box score being 0.5 and AD a score of 0.5 or 1. For the last test, result depended on education. CH participants had a score $\geq 9$ for 16 years of education, $\geq 5$ for 8 to 15 years of education and $\geq 3$ for 0-7 years of education. In the other hand, MCI and AD subjects had to have a score $\leq 8$, $\leq 4$ and $\leq 2$ for the same education groups[33].

#### *Outcome*

Throughout this article, we will refer to the evolution of clinical diagnostic categories as trajectory types. For instance, a subject with a MCI diagnostic at their first and last MRI was considered "stable" (MCI-MCI) while another who developed AD at a later stage would be a "converter" (MCI-AD).

### MRI data

#### *NOMIS*

Each NOMIS participant had an available T1-weighted MRI. Because the origin of the data is multiple, the protocol, MRI manufacturer and magnetic field strengths used were not uniform throughout the sample. Regarding manufacturers, 1,160 scans (18.60%) were made with a Philips Medical Systems MRI (Best, Netherlands), 3,853 (61.77%) with a Siemens Healthcare (Erlangen, Germany) scanner and 1,224 (19.63%) using GE Healthcare's products (Milwaukee, WI). Of these scans, 4,778 were done at magnetic field strengths of 3.0 Tesla and 1,459 at a field of 1.5 Tesla.

Part of the data used in the preparation of this article were obtained from the Parkinson's Progression Markers Initiative (PPMI) database. For up-to-date information on the study, visit www.ppmi-info.org.

#### *ADNI*

Participants were scanned on different MRI units albeit with a standardized protocol[34]. In total, there were 7414 scans and 4157 of those from MCI individuals at baseline. From those, the distribution of scans was similar to NOMIS with 547 (13.16%) using Philips Healthcare products, 2048 (49.26%) on Siemens Medical Systems units and 1562 (37.58%) on GE Healthcare. MRIs were taken with two field strengths; 2157 at 3.0 Tesla and 2000 at 1.5 Tesla. The age distribution was similar between MCI-AD (range: 55.1-95.9 y/o; average 76.1, SD 7.2 y/o) and MCI-MCI indviduals (range: 55.2-97.4 y/o; average 74.6, SD 7.7 y/o). For a full list of ADNI's subjects, refer to Supplementary Table S3 to S5.

#### *ADNI pre-processing*

ADNI being a longitudinal, multi-centric study, some subjects were scanned every six months while others every year, with different lengths of follow-up (median of 10.2 months, mean of 11.04 months and a standard deviation of 7.8 months). Thus, before being processed, ADNI longitudinal data was binned into standardized time step of 1 year (+/- 5 months), based on the distribution of time steps in the index. This process and its impact on the data is documented in Supplementary Figures S1 to S4. This served to make trajectories comparable among participants. Further, in ADNI1/GO, some participants were scanned initially at a field of 1.5T, but at every other follow-up at 3.0 T. In these cases the first scan was discarded in order to not bias morphometry estimates by scanner and field strength changes. In fine, the ADNI sample consisted of 1780 scans from 549 MCI subjects with at least one follow up, an average age of 74.6 (7.8) y/o for the MCI-MCI and 76.8 (7.3) y/o for MCI-AD. The distribution of regularized time steps had a median of 1.01, a mean of 1.00 and a standard deviation of 0.14.

#### *Image processing*

Each T1-weighted MRI was processed using *FreeSurfer* version 6.0, a free open-source software used to quantify brain anatomy. *FreeSurfer* encompasses multiple brain atlases to produce brain segmentation. We selected the Desikan-Killiany-Tourville atlas[35] (DKT, aparc.DKT.stats file) for the cortical segmentation and the automatic subcortical segmentation atlas (Aseg)[36]. The MRI data were processed using the "recon-all -all" command in *FreeSurfer* with the fully automated directive parameters (no manual intervention or expert flag options) on the CBRAIN[37] platform to extract thicknesses for all defined atlas regions.

The processing techniques used by FreeSurfer[17] to generate the cortical models consisted mainly of motion correction, removal of non-brain tissues using watershed/surface deformation procedure, automated Talairach transformation, intensity normalization, tessellation of the gray matter white matter boundary, automated topology correction, and surface deformation following intensity gradients to accurately place the tissue boundaries between gray/white matter and gray/cerebrospinal fluid. Additional processes are available following the cortical model : surface inflation, registration to a spherical atlas and parcellation of the cerebral cortex into units. These allow for a better representation of cortical thickness by using the intensity values and the whole information from the volume segmentation. Thickness is calculated using the closest distance from the gray/white boundary to the gray/CSF boundary at each vertex on the tessellated surface[26].

For this project, we used the average regional cortical thickness per region as a proxy of cortical neuronal degeneration, as validated in the work of Cardinal and Belathur[38,39]. This average was turned into a Z-score using the NOMIS tool, which normalizes the data based on a two-step regression model taking first into account image quality and head size (eTIV), then sex. Since age is an important factor in AD it was not used here to normalize data. Hence, for each participant, expected measure values were generated in the form of z-scores that demonstrate deviations from the normative NOMIS values.

## Data analysis

### *Low dimensional reduction*

According to the DKT atlas, the cortex was divided in 31 regions for each of the left and right hemispheres, and hence each data point was represented by a 62-dimensional vector. To facilitate predictive modeling, dimensional reduction of the data with UMAP was an important step. UMAP is a nonlinear algorithm based on Riemannian geometry and algebraic topology used for dimension reduction of high-dimensional datasets. To accomplish this, UMAP first computes the topology of the manifold as a $k$-nearest neighbor graph. The graph is weighted by the probability that two points are connected based on their distance computed with the Riemannian metric. The further two points are from each other, the least probable they are to be connected. For a given node, the number of nearest neighbors with which distances can be calculated are determined by the parameter `n_neighbors`, denoted by $k$ in the mathematical and computer science literature[27,28]. Then, UMAP tries to project the data on a lower euclidean dimension respecting the minimal possible distance between points in this space, given by `min_dist`. Finally, the topological graph is generated for this space, and by optimizing the cross-entropy between the lower and higher dimension topology, the algorithm finds the projection that represents the most the data topology[40](further details are included in McInnes[27]).

We first generated a low-dimensional manifold using UMAP by reducing the 62-dimensional cortical thickness data from NOMIS to $m$-dimensions (UMAP0, UMAP1, ..., UMAP$m-1$), where $m \ll 62$, using `min_dist` $= 0$ and different `n_neighbors` values of 2 to 1000 (Figure 3, Figure 4). We initially verified if $m = 2$ or $m = 3$ was the better target dimension for our problem. To do so, the explained variance of each dimension was calculated to verify if the third dimension was useful. We then used the trained model to transform each ADNI datum in the new $m$-D space.

### *Transformation for axis analysis*

In this application of the nonlinear UMAP method, it is difficult to interpret axes in terms of the features (thickness of cortical regions). Remark that algorithms such as PCA provide a linear combination of features to generate axes, while with UMAP these relations come from correlations. Moreover, the UMAP embedding doesn't impose an orientation on the data and thus, any rotation is equally valid. Therefore, after having applied the UMAP algorithm, we used a linear transformation over the UMAP embedding to rotate the data such that its principal axes could explain most of the variance in the embedding. This method allowed us to determine which features correlated the most with UMAP embedding axes. These transformed axes are referred to as t-UMAP. Because NOMIS is composed of cross-sectional data collected along a large age range (18 to 100 y.o.), we tested whether the algorithm implicitly embedded age in its representation. To test this, we used Pearson's correlation between age and t-UMAP vectors. We further tested if there were correlations between the axes and the thickness of the different brain regions.

### *Clustering*

The low dimensional t-UMAP space was then parcellated into data clusters each containing the same number of data points, in order to achieve similar statistical power in our trajectory analyses. To this end we adapted *scikit-learn*'s $k$-means algorithm[41] to our need of segmenting the data in equal groups.

A number of clusters ($C$) can be specified by the user and the number of data points in each cluster ($n$) is the determined from the overall size of the data set. The clusters' centroids were initialized using *scikit-learn*'s $k$-means++ algorithm[42]. A distance matrix between each points and centroids was then computed, and a probability matrix calculated. The entries of the latter matrix describe the probability that a given data point (row) belongs to a given cluster (column). These probabilities are based on the distances between data points and the centroids according to the formula: $\mathbf{W}_{ij} = 1 - \mathbf{D}_{ij}/\mathbf{V}_i$ where $\mathbf{W}$ is

the probability matrix, **D** is the distance matrix and **V** is a column vector where each element is the maximum value of the corresponding row in **D**. The matrix entry has a value of 0 if the corresponding centroid is the furthest from the data point.

For each cluster, the $n$ likeliest points were then assigned to it. If the number of data points was not divisible by $C$, the unassigned data points were assigned to their likeliest cluster.

An iterative process followed, in which, at each iteration, centroids' position and their distances from every point were calculated; probabilities for a point to switch cluster are ordered; and assignments performed. The process was run until the inertia (within-cluster sum-of-squares of the distances between points and their closes centroid) could not be minimised further, or a maximum number of iterations was reached[41].

### Probabilistic Trajectory

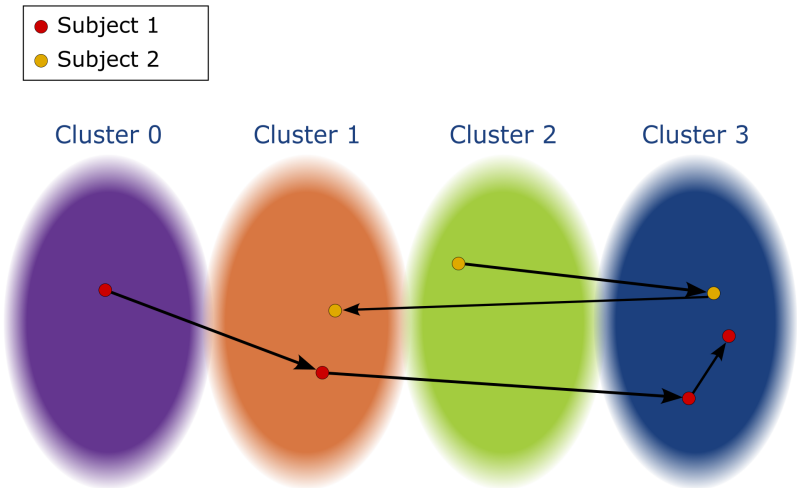


**Figure 2.** Defining trajectories. An arbitrary embedding with four clusters. The arrows represent the direction in time for each subject. Given an embedding with clusters we can define the longitudinal trajectory of subjects as follow. In this example, subject 1 would have a full trajectory of [0-1-3-3] while subject 2 [2-3-1]. The trajectory of length 1 would be [3] for subject 1 and [1] for subject 2 and the trajectory of length 3 would be [1-3-3] for subject 1 and [2-3-1] again for subject 2. Subject 2 wouldn't have a trajectory of length 4 and subject 1's would be equivalent to its full trajectory.

In the $m$-dimensional space computed from NOMIS data, we projected the ADNI data points and segmented them into identical-size clusters, after which we turned our attention to the problem of trajectory prediction.

We first defined as trajectory the ordered sequence of clusters through which a participant's data belonged in its longitudinal course. Figure 2 shows a simplified representation of an embedding with four clusters. As shown in the figure, we defined a subject's trajectories from their latest data point, meaning a trajectory of length 3 is composed of the 3 oldest datum for a subject. To characterize trajectories at the group level, in every possible trajectory we computed the probability that an individual in this trajectory developed AD. First, given an embedding with $C$ clusters, the total number of trajectory $T$, for every possible trajectory of length one to $L$, is given by $T = \sum_{l=1}^{L} C^l$. Each $T$ trajectory are initialised with a null probability. The probabilistic atlas is then generated, in which every entry was composed of a trajectory and its associated AD progression probability. Then, for every participant, we pieced together cluster trajectories for the last, two last and three last data points, thus creating trajectories of length one, two and three steps for the participants. Depending on the final diagnosis at the last step (i.e. whether the participant remained stable or progressed to AD), the probability of this trajectory with respect to AD was updated consequently. Once the whole dataset was processed, we then had an atlas tying the probability of developing AD to each possible trajectory of length 1 to 3.

A disadvantage of this approach is that empty trajectories (paths not taken by any participant) were evaluated as paths with a probability of zero, even though no data were available. These trajectories cannot be tossed aside since future participants might follow such trajectories, and a statistic will be required to "predict" diagnosis. We then arbitrarily chose for these trajectories to remain at a value of zero.

Given that ADNI has 949 MCI individuals at baseline, $C^l$ must be $\ll 949$ so that trajectories of length $l$ are reasonably populated. Because of this limitation, we empirically limited the length of a trajectory to the last three data points (i.e. three years before diagnostic of AD) and the maximum number of cluster to 7, which gave us a maximum of 343 unique trajectories. Since the subjects are not uniformly distributed between every trajectory, as shown in Supplementary Figure S5 and S6, we

could afford $C^l$ to be $\approx 1/3$ of the number of subjects. Indeed a lot of trajectories will never be used and can thus be discarded. Supplementary Figure S5 shows that $C = 7$ and $l = 3$ gives 108 used trajectories. Given larger datasets, these limitations could be lifted.

### Statistical analysis

We performed a sensitivity analysis as follows. First, we randomly assigned ADNI participants into training (90% of MCI-MCI (321 individuals) and 90% of MCI-AD (206 individuals)), and test (remaining) groups. Both groups were projected in the transformed UMAP space, created by the NOMIS dataset. The cluster segmentation algorithm was then applied on the training group, before computing the probabilistic atlas as defined above.

We then extracted the final results using the test group. For each participant, we calculated the probability of progressing to AD given their last 1, 2 and 3 data points. We then set an arbitrary threshold to binarize predictions (e.g. every prediction with a probability higher than a threshold of 0.5 would be qualified as an AD subject). We computed a receiver operating characteristic (ROC) curve for each trajectory length (1, 2, or 3) by varying the value of this threshold from 0 to 1, calculating the true positive rate ($sensitivity$), false positive rate ($1 - specificity$) and area under curve (AUC).

To verify the predictive power of these curves, we resampled the train and test subsets 2000 times using a different random seed. The ROC curves and AUC were recalculated at every iteration.

## Results

### UMAP transformation

Using UMAP on the standardized NOMIS data, we explored different embedding possibilities as a function of `n_neighbors` values. Figure 3 shows this impact. Each embedding encompasses a strong correlation between the first (UMAP0) axis and age, as shown by the color gradient. However, for high `n_neighbors` values, changes in the embeddings were less prominent. For instance, Figure 4 shows that the correlation between t-UMAP0 and age varies only slightly after `n_neighbors` = 5.

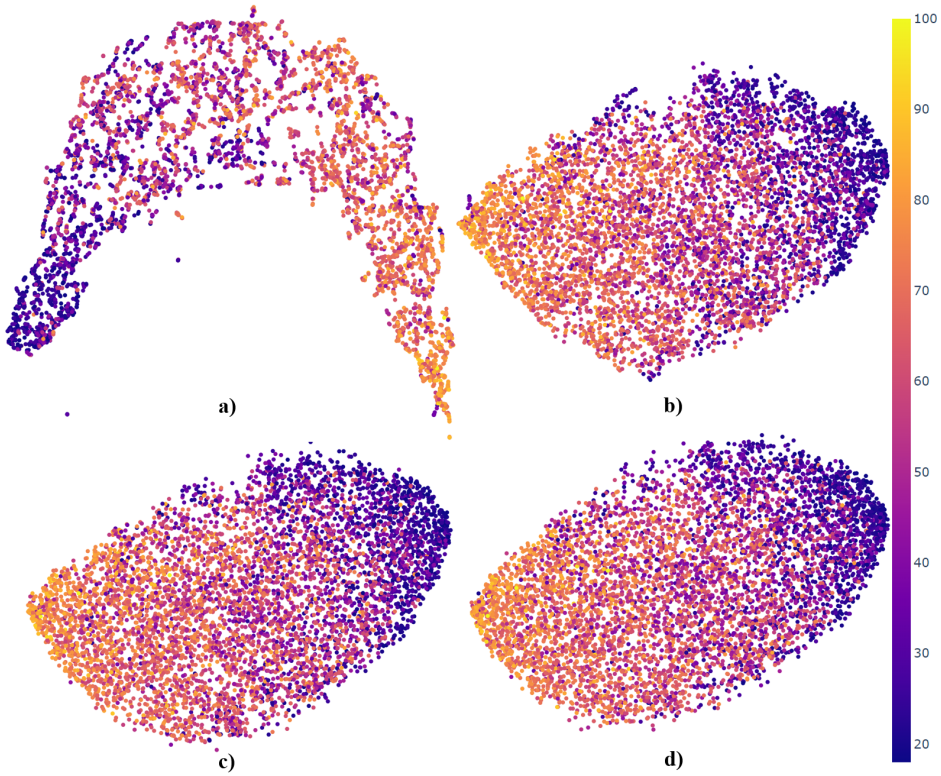


**Figure 3.** UMAP embeddings of the NOMIS database using four different values of `n_neighbors`. The age (years) of the participants is color coded. The parameter `min_dist` = 0 for all embeddings. Figure 3**a)** has `n_neighbors` = 3, Figure 3**b)** has `n_neighbors` = 20, Figure 3**c)** has `n_neighbors` = 100 and Figure 3**d)** has `n_neighbors` = 1000. Note that axes have been scaled to fit every point in the frame.

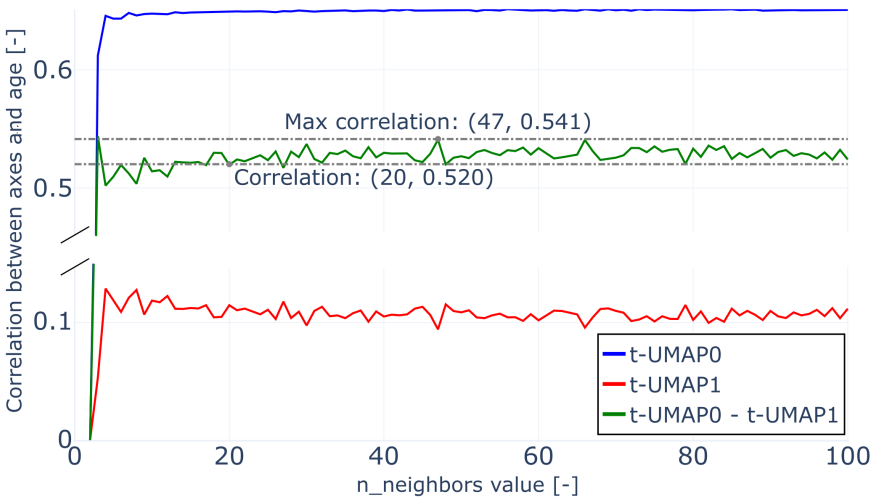


**Figure 4.** Choice of embedding. The correlation between the axes t-UMAP0 (in blue) and t-UMAP1 (in red) with the age of NOMIS' subjects. In green is the difference between the blue and the red line, to show the embeddings that maximise t-UMAP0's while minimizing t-UMAP1's correlations with age. The dashed lines show the maximum and minimum value of the green line after `n_neighbors`=20, value at which the variations in correlation are mostly constrained between these minimum and maximum.

To select the embedding for our trajectory analysis, we computed the correlation between t-UMAP0 (blue) and t-UMAP1 (red) with the age of NOMIS subjects when varying the parameter `n_neighbors`, shown in Figure 4. For t-UMAP0 and for low values of `n_neighbours`, the correlation steeply increases as `n_neighbors` increases before quickly converging towards an asymptote. The correlation between age and t-UMAP1 also seems to converge to an asymptotic value albeit in a more noisy fashion. Hence, to choose the optimal `n_neighbors` value we wanted to maximise correlation between t-UMAP0 and age, while minimizing the one between t-UMAP1 and age. The green line of Figure 4 shows the difference between these relations. We discarded the first maximum (`n_neighbors`=3) since the correlation with t-UMAP0 was not maximised. Optimal correlations were contained between `n_neighbors`=20 and `n_neighbors`=47, meaning that differences were most likely due to random noise. Therefore, to preserve computer resources and the local structure of the underlying manifold, we chose `n_neighbors`=20 as our embedding of interest for this study. It is of note that we also tested higher dimension embeddings. Using a 3-dimensional embedding with `n_neighbors`=20, we computed the explained variance of each dimension to quantify the usefulness of each dimension. It was shown that the first dimension explained 95.91%, the second 2.93% and the third 1.16% of the variance. We felt therefore justified in working with the first two dimensions.

### Reorientation of UMAP embedding along its principal axes and correlations

Once the embedding's axes are align with the principal axes, we noticed that participants' ages correlated with the transformed main UMAP axis (t-UMAP0; $r = 0.65$), as shown on Figure 5. It has to be noted that chronological age was not used as an input in the UMAP transformation and this is therefore an emergent property of the embedding. There were six brain regions that were heavily negatively correlated with t-UMAP0 : superior frontal gyrus ($r = -0.88$), supramarginal gyrus ($r = -0.85$), inferior parietal gyrus ($r = -0.83$), rostral middle frontal gyrus ($r = -0.83$), caudal middle frontal gyrus ($r = -0.82$) and superior temporal gyrus ($r = -0.81$). As for t-UMAP1, the peri-calcarine ($r = 0.55$), the cuneus ($r = 0.48$) and the lingual gyrus ($r = 0.47$) were the three regions with the highest correlation. One notices in Figure 5 how the older ADNI participants (age at entry > 65 y.o.) preferentially concentrate along the positive t-UMAP0 direction, congruent with its correlation with age in the NOMIS dataset. For further information, consult the Supplementary Tables S1 and S2 displaying the full extent of the correlations between cortical regions and t-UMAP0 and t-UMAP1.

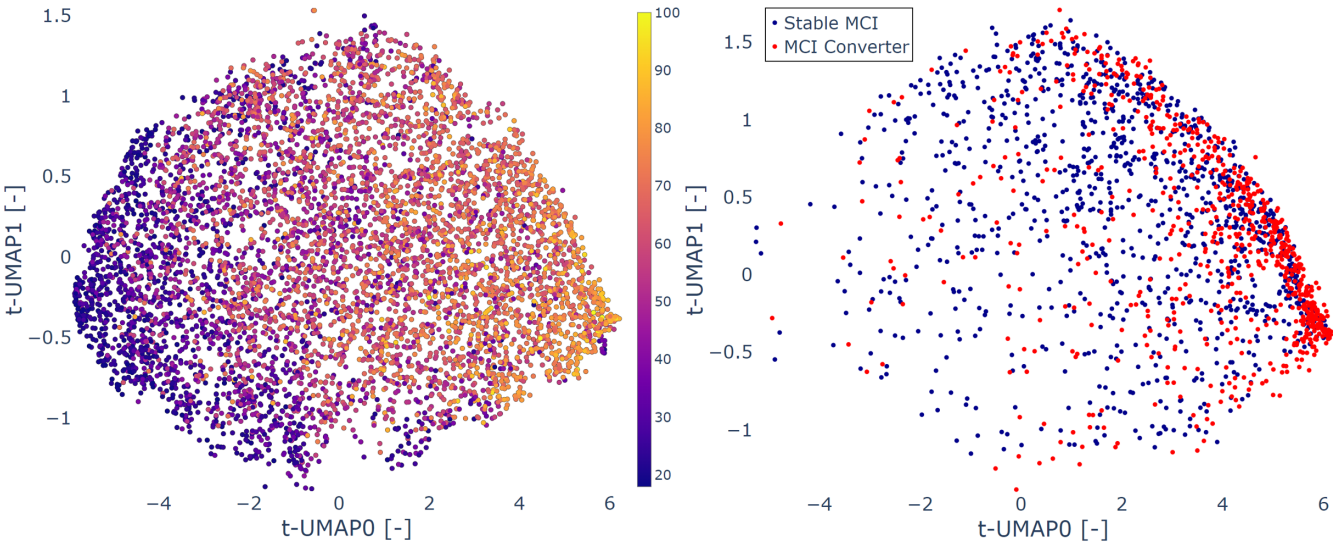


**a)** NOMIS embedding, color coded for age at scan **b)** ADNI data color coded for the final diagnosis

**Figure 5.** Transformed UMAP embedding and fitted ADNI data. Linear transformation applied on the UMAP embedding with `n_neighbors` = 20 to align the principal axes with UMAP0 and UMAP1. In **a)**, the NOMIS database (embedding data) with participants' chronological age (years) at scan color-coded using the color scale displayed on the right. In **b)**, participants from the ADNI database were projected in the NOMIS-defined UMAP embedding. Subject's final diagnosis was used to color the points on **b)**. One notices how the older ADNI participants (age at entry > 65 y.o.) preferentially concentrate along the positive t-UMAP0 direction, congruent with its correlation with age in the NOMIS dataset.

### Trajectories

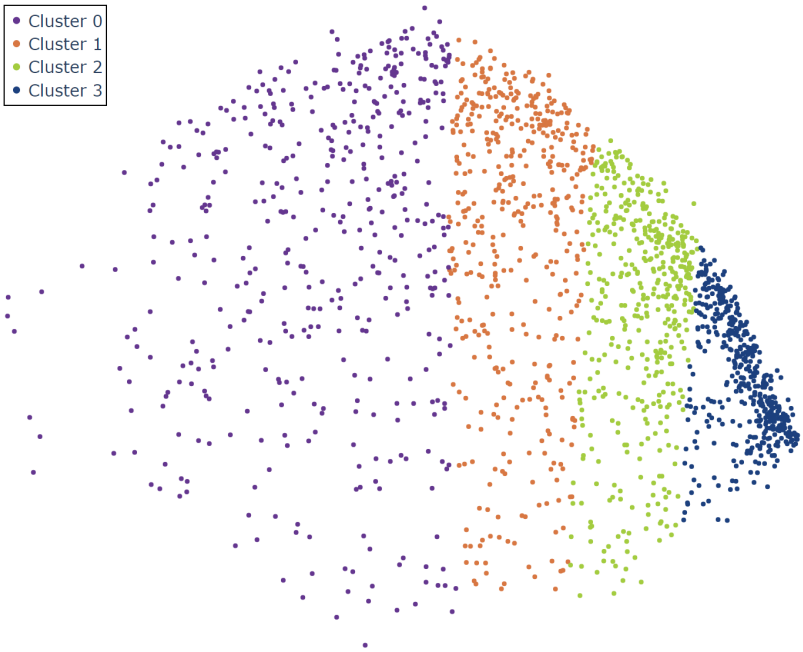


**Figure 6.** Clustering of the ADNI embedding with same size *k*-means. Dimensional reduction of the ADNI database using a linearly transformed UMAP model trained on the NOMIS database using `n_neighbors` = 20 and `min_dist` = 0. The four colors represent the clusters made from the positional values, using a variation of the *k*-means algorithm with `n_clusters` = 4. For simplicity's sake, the axes are not displayed since they are the same as Figure 5

To get the trajectory of each individual, we first separated the ADNI dataset into the training data, projected it in the NOMIS t-UMAP space, and separate this embedding into clusters. In Figures 6 and 7, we used the same_size cluster algorithm defined in the section *Clustering* with `n_clusters`=4.

For illustrative purposes we show in Figure 7 how different participants move through the embedding with time (a "trajectory"). We see that ADNI participants tend to move in a positive direction along t-UMAP0, i.e. from clusters on the left (clusters 0 and 1) to those on the right (clusters 2 and 3) as they age. Some subjects have a direct trajectory to the right-most cluster (solid line in Figure 7a) and small dashed line in Figure 7b) ), while others have a more convoluted path (dotted line in Figure 7a and 7b). On the other hand, some participants move from right to left (not displayed on 7, see 8), in the negative t-UMAP0 direction.

Figure 7c demonstrates the trends for the average MCI-MCI and MCI-AD groups. Notably, MCI-AD subjects whose trajectory initiates in cluster 3 tend to remain in this cluster, while MCI-MCIs move back towards cluster 2. Also, MCI participants whose trajectory initiates in clusters 1 and 2 display shorter movement towards the right for MCI-MCIs and a greater movement in this direction for AD. Thus, there seems to be an attraction towards a center of mass in cluster 3 for ADs, and in between clusters 1 and 2 for MCI-MCIs.

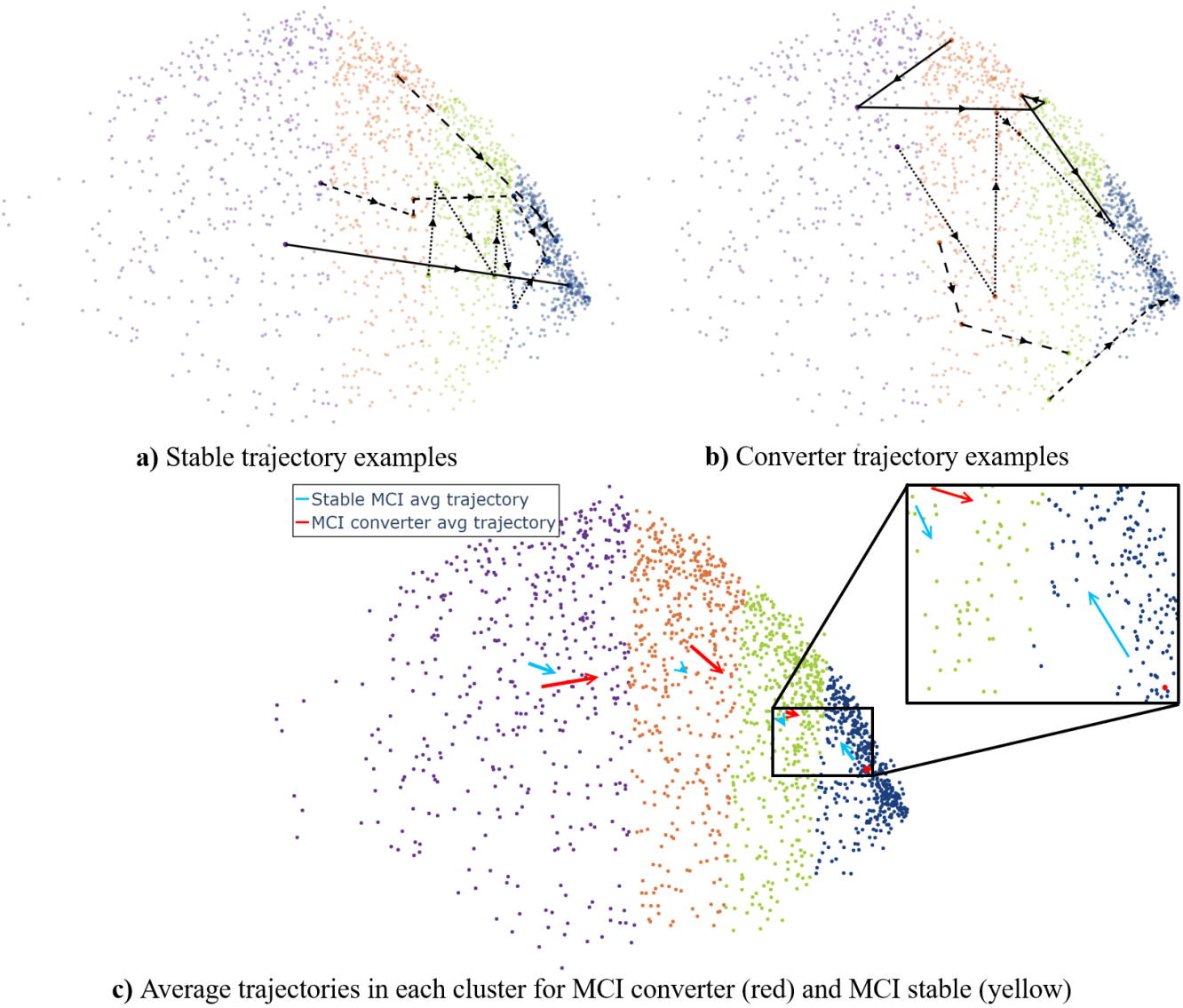


**a)** Stable trajectory examples

**b)** Converter trajectory examples

**c)** Average trajectories in each cluster for MCI converter (red) and MCI stable (yellow)

**Figure 7.** Individual and average trajectories for MCI-MCI and MCI-AD subjects. UMAP model shown in Figure 6 with individual trajectories for four MCI-MCI subjects (Figure 7a) and four MCI-ADs (Figure 7b). Different dashed lines are used to differentiate between different subjects and the arrows point in the direction of time. Figure 7c) shows the average trajectories for both types of trajectories. In cluster 3, MCI-ADs are represented by a point because the trajectory is too short to be represented by an arrow.

Figure 8 displays the probabilistic atlas in its entirety. Using the embedding and clusters from Figure 6, we computed the proportion of individuals having converted to AD in each possible trajectory of length 1, 2 and 3, using participants' last $l$ data points. This allows us to make some further observations on the trajectories. First of all, there seems to be a relationship between the last cluster being visited and prognosis. For instance, trajectories 0 ; 0-0 ; 0-0-0 have a very low probability of developing AD ($< 18\%$), while trajectories 3 ; 3-3 ; 3-3-3 have a probability between 62% and 77% to be converting MCIs, with intermediate clusters displaying a progressive relation. Secondly, out of the 56 trajectories with at least one subjects, 30 were monotonically increasing or stable (i.e. moving from lower to higher cluster ID or staying in the same cluster). These seem to follow the previous phenomena related to aging and eventual conversion to AD. The second half of trajectories (n = 26) were more random. However, it is of note that the population distribution for these trajectories have a median of three subjects; while the five trajectories with 10 or more subjects all had an associated conversion probability of under 42%. Thus, they seem more representative of either noisy data or morphological variability without association to conversion. Moreover, trajectories that have a point in cluster 3 without finishing in it have all probabilities $\leq 50\%$ and are more populated than most of the abnormal trajectories ; with a median at 4, a mean at 6.6. This shows that these trajectories are more often associated

with MCI even thought this cluster is by itself more associated with the AD. Finally, there are a number of outlier quadrants with either a probability of zero or one, due to a limited sample size (1 to 3 subjects).

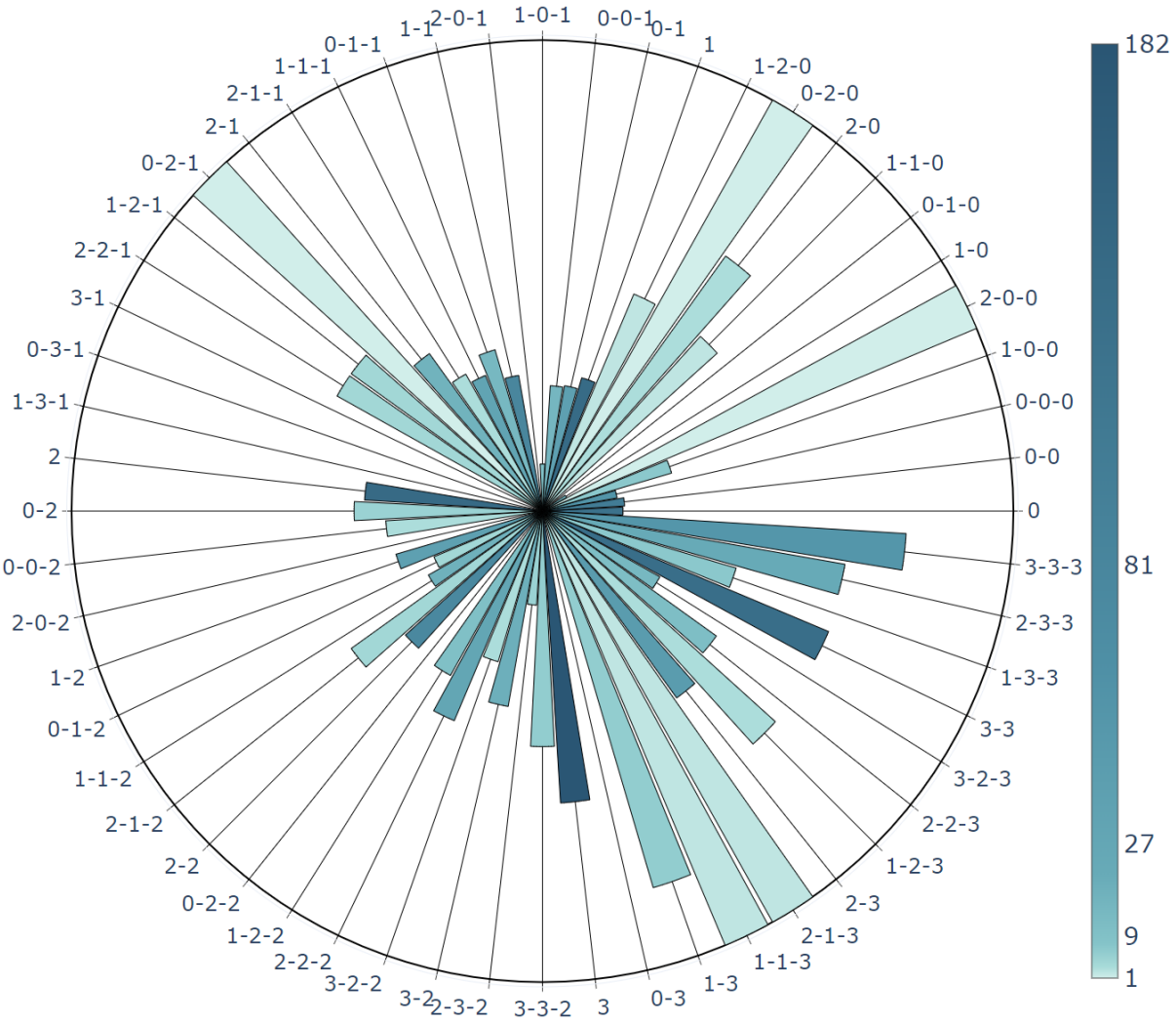


**Figure 8.** Probabilistic atlas. The distribution of the proportion of AD subjects in each trajectory of size 1 to 3, color coded for the population in each trajectory. For the sake of visibility, unpopulated trajectories are not displayed.

## ROC curves

We computed the AUC of our ROC curves as an indication of the efficiency of our probabilistic atlas at classifying the test group. Using a random training group containing 90% of every MCI-MCI and 90% of every MCI-AD participant, we computed the probabilistic atlas for trajectories of length 1, 2 and , by using the previously mentioned dimensional reduction method and clustering method. The 10% of data left was used to test the accuracy of our method. Varying the threshold probability value at which the participant was deemed to convert allowed us to generate ROC curves shown on Figure 9.

This process was repeated 2000 times with different random seeds to split the dataset into training/testing sets. The average and standard deviations for this AUC distribution were calculated and are displayed as a table insert in Figure 9. We notice that accuracy grows as a function of `n_clusters` for a given length, with the most accurate models at `n_clusters`=5, and a plateau at `n_clusters`=6. The accuracy of our method did not change significantly between `n_cluster`= 6 or `n_cluster` = 7, regardless of trajectory length.

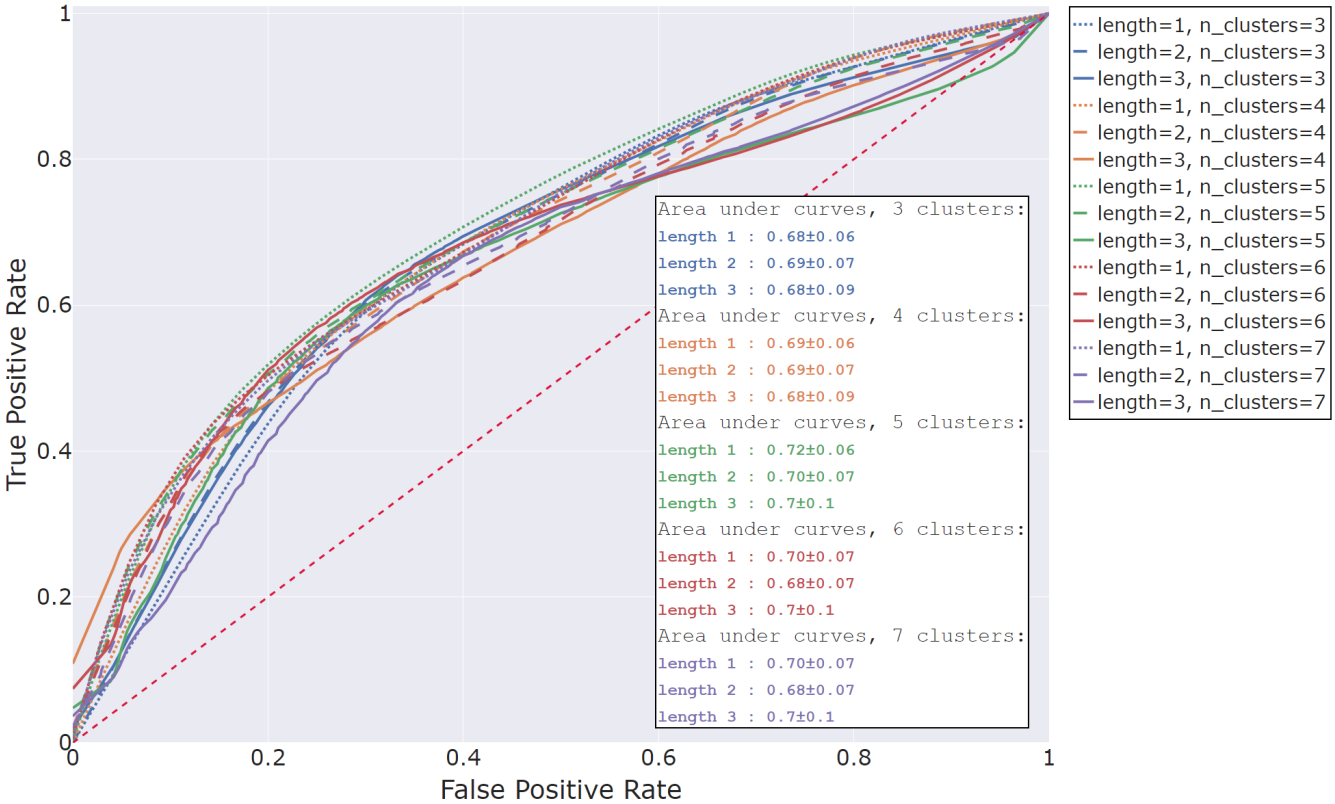


**Figure 9.** ROC curves of 5 different clustering of the transformed UMAP embedding (with 3, 4, 5, 6 and 7 clusters). For each clustering, predictions are made using trajectory length of 1, 2 and 3 last time points. The dashed red line represent the diagonal with area under curve (AUC) of 0.5 for reference. The AUC of each ROC curves is displayed in the table at the bottom right of the figure. This value is obtained by averaging the AUC from 2000 resamplings of the train/test subsets and the value following the $\pm$ is the standard deviation of this distribution. Moreover, the ROC curves displayed are obtained by averaging the ROC curves from 2000 resamplings.

## Discussion

Our goal in the present work was to investigate low-dimensional representations of aging trajectories in order to identify differences between trajectories related to healthy or stable cognition and decline due to probable AD. We wanted to develop a method that has a good predictive accuracy, but that at the same time, remains interpretable. To do so, we first extracted a vector of cortical thicknesses of different brain regions using FreeSurfer. We then further reduced the dimensionality of the data using the nonlinear method UMAP and linearly transformed the UMAP embedding while maximizing the correlation of the main axis with age. We then investigated the different aging trajectories in this transformed UMAP space and found out significant differences between MCI-MCI and MCI-AD trajectories. We estimated that our novel approach could yield a good predictive accuracy, with a maximum AUC of about 0.72. We now discuss the novelty of our approach, its limitations and possible future research directions.

### UMAP as a nonlinear embedding technique

UMAP was chosen over PCA since the former provided a more compact and homogeneous embedding of the data, with a lesser standard deviation in both the $x$ and $y$ axes, which is advantageous when dividing the space into clusters of similar size. Also, as previously mentioned, the nonlinearity of UMAP is advantageous as it represents more accurately cortical thickness atrophy happening with age, while preserving both local and global features of the original high-dimensional dataset. The optimization of UMAP parameters required us to fix `min_dist` to 0. This means that two MRIs yielding the same image will occupy the same position in the t-UMAP space. This is useful for us since it will induce a positive distance between two points only if they are different, and thus a participant's trajectory is not artificially modified. Furthermore, two similar points are more likely to be in the same cluster. Then, for the parameter `n_neighbors`, Figure 3 showed the different embeddings given a value of the parameter. As explained in the UMAP paper[27], lower values make the embedding locally connected while higher values make it globally connected, meaning that global structures in the data are represented over local ones. The figure represents this by showing the softening of internal structures for high `n_neighbors` values. Indeed, for the lowest value of `n_neighbors`, the embedding takes a very different form. With low values, local resemblance between members of the NOMIS database are put forth while the more `n_neighbors` is high and the more the embedding starts looking alike : points are uniformly distributed inside an ellipsoid. For the current paper, we prioritize global structures since embeddings with lower `n_neighbors` are less suitable for the same reason PCA was not. Moreover, we chose the correlation between t-UMAP0 and subject's age as a metric of how much the embedding encompasses the aging process. Figure 4 shows that this value is optimized from `n_neighbors` = 20. In light of this, we chose the embedding with `n_neighbors` at 20 since it offered a good compromise between local and global structures and the correlation with age is optimized for all axes (Figure 4). Finally, before settling on a two-dimensional representative space, we verified that a higher-order embedding would not better fit the data. The explained variance of the third dimension (1.16%) showed that the first two dimensions were sufficient to represent our datasets.

### Age dependency

Applying a linear transformation on the embedding in order to align the principal axes with the UMAP0 and UMAP1 axes yielded a new space where the t-UMAP0 axis correlated the most with the age. Indeed, the age gradient on Figure 5 seems to progress parallel to the axis. Thus, younger individuals are located leftmost of the figure while older ones are on the right. In a way, the t-UMAP0 axis can be interpreted as a participant's "brain age"; the fact that some younger participants had a strong "positive" brain age is indicative of individual variability. Note however that *FreeSurfer* seems to introduce significant noise in morphometric measurements, which causes highly variable trajectories for some individuals.

It is of note that, in this paper, we specifically chose to use a dataset of healthy individuals with a wide age range to train the UMAP embedding. This was done with the idea that the embedding would encompass the normal aging process which would make it easier to differentiate AD trajectories down the line. In a way, it is what we were able to do since the embedding correlates with the brain age of subjects. Interestingly enough, the data is relatively uniformly distributed in the embedding and no clearly defined clusters are present. This shows again that UMAP wasn't able to find defined characteristics in the data and so every subject is represented in a spectrum of the aging process. Moreover, we chose to use no prior to select the features to be reduced. This again goes with the idea we wanted the embedding to represent the aging process of the brain. For the specific purpose of predicting decline, we could have used *Dickerson* et *al.*'s cortical AD signature[7] to select specific AD related regions, which would have helped increase the sensitivity of our model and hence its predictive power. On that note, the inferior parietal and superior frontal gyrus are both heavily correlated with the t-UMAP0 axis and have been identified as regions within the AD signature[7].

### Trajectory definition and analyses

As for the trajectories, from Figure 7c) it is clear that MCI-MCI trajectories are different from MCI-AD. Indeed, both trajectory types have different attracting points and different average trajectories, as mentioned in the previous section, although it could

be construed that most of these differences between trajectory types could be explained by the differences in the samples represented in each type. For example, the distributions can be different because AD usually appears with old age, meaning that it is expected for the MCI-AD distribution to be slanted to the right, since the t-UMAP0 axis correlates with the age. In our case, ADNI's MCI-AD and MCI-MCI subjects have a similar age distribution, both with an average age of 76 and 75 y/o, a standard deviation of 7.2 and 7.7 y/o respectively and similar values of minimum (55.1 and 55.2 y/o) and maximum age (95.9 and 97.4). Thus, it is clear that the difference in the trajectory is caused by an inherent global difference in cortical thickness between MCI-MCI and MCI-AD participants that underlines the embedding. This statement also relates to the difference in average trajectory direction and norm. For MCI-MCI subjects, we see in Figure 7c) that these trajectories are attracted towards the lower end of cluster 2 while MCI-MCIs are clearly attracted to cluster 3. In this cluster, we observe that MCI-ADs have an average trajectory nearly null while MCI-MCIs tend to escape the cluster towards their point of attraction. Moreover, AD subjects move more towards cluster 3 than MCI-MCI, as shown by the length of the vectors, showing again a difference in attraction between the two types of aging process. Evidently, it shows that the t-UMAP space is able to differentiate MCI-MCI's brain trajectory from AD's and these are reflected on the figures by the difference in distribution, flux and attracting points.

Figure 7a) and 7b), on the other hand, shows similarities between MCI-MCI and MCI-AD trajectories. Indeed, both trajectory types can end up in the rightmost cluster, and follow similar paths. Since some MCI-MCI have unfinished follow-ups, a portion of them could turn out with AD. For instance, following the observations made in the previous paragraph, a MCI in cluster 3 could eventually become an AD and stay in the cluster or stay stable and go back towards cluster 2. This uncertainty relating to the final diagnosis of MCI-MCI decreases the accuracy of the average trajectories in Figure 7c) and of the predictions of Figure 8 and 9. Furthermore, some subjects perform alternative sharp turns while moving towards cluster 3. Following the observations made previously, we know that the t-UMAP1 axis correlates strongly with the thickness of several brain regions (superior frontal gyrus, supramarginal gyrus, inferior parietal gyrus, *etc.*). In that way, the sharp variations (shown with dotted lines in Figure 7a) and 7b)) do not make biological sense, since it would mean that the thickness of these brain regions goes up and down as subjects age. Yet again, this is most likely a result of *FreeSurfer's* noisy estimation of morphometric features. Extensitve quality control of a subject's morphometric data should be done if one is to use such a technique for individual predictions.

### Clusters

Some interesting patterns emerge in the atlas shown in Figure 8. First of all, there is a strong relationship between the final cluster and AD diagnosis. Indeed, trajectories with the most subjects show a trend where subjects with a final scan in cluster 0 have a low ($\sim$ 17%) probability of developing AD and the probability goes up with the index of the final cluster : cluster 1 $\sim$30%, cluster 2 $\sim$38% and cluster 3 $\sim$62%. Moreover, the longer a subject stays in the cluster the stronger is this trend. For example, the 3-step trajectory "0-0-0" has a similar probability than its homologous 1-step trajectory "0", while "1-1-1" shows a $\sim$2% increase in probability when compared to "1", "2-2-2" a $\sim$10% increase when compared to "2" and "3-3-3" a $\sim$15% increase when compared to "3". Since we know age is distributed similarly between AD and MCI-MCI subjects, there seems to be a clear relationship between cluster 3 and the diagnosis of AD. Moreover, trajectories with an intermediary data point in cluster 3 and another in cluster 0, 1 or 2 afterwards, have a significantly lower probability to describe AD. This phenomenon is directly related to our observations that MCI-MCI subjects in cluster 3 go towards the other clusters on average, while AD subjects stay in cluster 3. From this figure we can then conclude the clusters and trajectories are correlated with certain diagnosis.

The predictive analysis shown in Figure 9 corroborates the previous observations. Indeed, the AUC shows that trajectories, based on cortical thickness only, are able to classify subjects between MCI-MCIs and MCI-ADs in more than 72% of cases for the best models (5 clusters). Moreover, for every model the essential information necessary for classification seems to be located in the last cluster of the trajectory, since longer trajectory length reduces the accuracy and enhances the standard deviation. We previously demonstrated that MCI-MCIs in cluster 3 return toward cluster 2 while MCI-ADs stay in cluster 3. This shows that a longer trajectory size can have a value for classification, but some trajectories add more noise and decrease the overall effectiveness of the prediction. The accuracy of the prediction is also influenced by the number of clusters, with the lower values (3 and 4 clusters) yielding lower results, 5 clusters the best predictive value and additional clusters have diminishing return. By increasing the number of clusters, the population in clusters 2 and 3 (in Figure 6) is divided into more clusters. There are then fewer subjects in each cluster, reducing the statistical significance of each trajectory and making the probability associated with each trajectory less accurate.

## Conclusion

This study explored the visualization and statistical analysis of morphometric aging trajectories using UMAP, a novel dimensionality reduction technique, for subjects with AD or a MCI. We demonstrated the potential advantages of using this approach. We showed that using this method leads to an embedding space whose principal axis is strongly correlated with

the chronological age of the individuals. This observation prompted us to apply a linear transformation to the UMAP space that maximizes the correlation between the principal axis and chronological age while minimizing the standard deviation. We then developed a cluster-based method to describe the trajectory of each subject. This method allowed us to demonstrate that MCI-MCI trajectories were significantly different from AD trajectories by showing that some sequence of clusters were more frequently observed in MCI-AD subjects. Moreover, subsampling the data enabled us to show that these trajectories can indeed discriminate between MCI-MCI and AD subjects, meaning that, it is possible to predict with a positive accuracy the final diagnosis of a subject based on its trajectory through the embedding. Our results thus indicate that UMAP is a new and effective tool to not only visualize aging trajectories, but also accurately differentiate between MCI-AD and MCI-MCI trajectories. To further improve the accuracy of the model, it would be of interest to perform a UMAP-based analysis using only the thickness of cortical regions related to AD[7,26,43] and other data related to AD biomarkers such as amyloid beta concentration[44,45], cognitive score[46] and cognitive reserve[47].

## Data availability statement

For the NOMIS and ADNI datasets, the data is publicly available upon request. The links to the different databases can be found in the acknowledgements and here :

Autism Brain Imaging Data Exchange (ABIDE): http://fcon_1000.projects.nitrc.org/indi/abide/

Alzheimer's Disease Neuroimaging Initiative (ADNI): http://adni.loni.usc.edu/

Australian Imaging Biomarkers and Lifestyle flagship study of ageing (AIBL) : https://aibl.csiro.au/

Berlin Mind and Brain (Margulies, Villringer) CoRR sample (BMB): http://fcon_1000.projects.nitrc.org/indi/CoRR/html/bmb_1.html

Cambridge Centre for Ageing and Neuroscience (CamCAN): http://www.mrc-cbu.cam.ac.uk/datasets/camcan/

Center of Biomedical Research Excellence (COBRE): http://fcon_1000.projects.nitrc.org/indi/retro/cobre.html

Cleveland Clinic (Cleveland CCF): http://fcon_1000.projects.nitrc.org/indi/retro/ClevelandCCF.html

Consortium for the Early Identification of Alzheimer's Disease (CIMA-Q): http://www.cima-q.ca

Dallas Lifespan Brain Study (DLBS): http://fcon_1000.projects.nitrc.org/indi/retro/dlbs.html

FIND lab sample: http://fcon_1000.projects.nitrc.org/indi/retro/find_stanford.html

Functional Biomedical Informatics Research Network (FBIRN): http://www.birncommunity.org/resources/data/

Lifespan Human Connectome Project in Aging (HCP-Aging): http://dx.doi.org/10.15154/1520138

International Consortium for Brain Mapping (ICBM): https://ida.loni.usc.edu/login.jsp?project=ICBM

Information eXtraction from Images (IXI): http://brain-development.org/ixi-dataset/

F.M. Kirby Research Center neuroimaging reproducibility data (KIRBY-21): https://www.nitrc.org/projects/multimodal

Minimal Interval Resonance Imaging in Alzheimer's Disease (MIRIAD): http://miriad.drc.ion.ucl.ac.uk

National Alzheimer's Coordinating Center (NACC): https://www.alz.washington.edu/

National Database for Autism Research (NDAR): http://nda.nih.gov

Nathan Kline Institute Rockland (NKI-R) sample (NKI-RS): http://fcon_1000.projects.nitrc.org/indi/pro/nki.html

NKI-R enhanced Sample (NKI-RES): http://fcon_1000.projects.nitrc.org/indi/enhanced/

Open access series of imaging studies (OASIS): http://www.oasis-brains.org/

POWER: http://fcon_1000.projects.nitrc.org/indi/retro/Power2012.html

Parkinson's Progression Markers Initiative (PPMI): http://www.ppmi-info.org

Southwest University Adult Lifespan Dataset (SALD): http://fcon_1000.projects.nitrc.org/indi/retro/sald.html

University of Wisconsin, Madison (Birn, Prabhakaran, Meyerand) CoRR sample (UWM): http://fcon_1000.projects.nitrc.org/indi/CoRR/html/uwm_1.html

Wayne State EF Dataset: http://fcon_1000.projects.nitrc.org/indi/retro/wayne_EF.html

Yale Low-Resolution Controls Dataset: http://fcon_1000.projects.nitrc.org/indi/retro/yale_lowres.html

## References


1. Maresova, P., Mohelska, H., Dolejs, J. & Kuca, K. Socio-economic aspects of Alzheimer's disease. *Curr. Alzheimer Res.* **12**, 903–911, DOI: 10.2174/1567205012091510191114 48 (2015).
2. Cimler, R., Maresova, P., Kuhnova, J. & Kuca, K. Predictions of alzheimer's disease treatment and care costs in european countries. *PLoS One* **14**, e0210958, DOI: 10.1371/journal.pone.0210958 (2019).
3. Pfefferbaum, A. *et al.* A quantitative magnetic resonance imaging study of changes in brain morphology from infancy to late adulthood. *Arch. neurology* **51**, 874–887, DOI: 10.1001/archneur.1994.00540210046012 (1994).
4. Giedd, J. N. *et al.* Brain development during childhood and adolescence: a longitudinal MRI study. *Nat. neuroscience* **2**, 861–863, DOI: 10.1038/13158 (1999).
5. Bernasconi, N. *et al.* Whole-brain voxel-based statistical analysis of gray matter and white matter in temporal lobe epilepsy. *Neuroimage* **23**, 717–723, DOI: 10.1016/j.neuroimage.2004.06.015 (2004).
6. Hedman, A. M., van Haren, N. E., Schnack, H. G., Kahn, R. S. & Hulshoff Pol, H. E. Human brain changes across the life span: a review of 56 longitudinal magnetic resonance imaging studies. *Hum. brain mapping* **33**, 1987–2002, DOI: 10.1002/hbm.21334 (2012).
7. Dickerson, B. C. *et al.* The cortical signature of Alzheimer's disease: regionally specific cortical thinning relates to symptom severity in very mild to mild AD dementia and is detectable in asymptomatic amyloid-positive individuals. *Cereb. Cortex (New York, N.Y.: 1991)* **19**, 497–510, DOI: 10.1093/cercor/bhn113 (2009).
8. Johnson, Fox, Sperling & Klunk. Brain imaging in alzheimer disease. *Cold Spring Harb Perspect Med* **2**, DOI: 10.1101/cshperspect.a006213 (2012).
9. Duchesne, S. *et al.* Mri-based automated computer classification of probable ad versus normal controls. *IEEE transactions on medical imaging* **27**, 509–520, DOI: 10.1109/TMI.2007.908685 (2008).
10. Ke, Q., Zhang, J., Wei, W., Damaševičius, R. & Woźniak, M. Adaptive independent subspace analysis of brain magnetic resonance imaging data. *Ieee Access* **7**, 12252–12261, DOI: 10.1109/ACCESS.2019.2893496 (2019).
11. Tang, Y., Chen, D. & Li, X. Dimensionality reduction methods for brain imaging data analysis. *ACM Comput. Surv. (CSUR)* **54**, 1–36, DOI: 10.1145/3448302 (2021).
12. Xifra-Porxas, A., Ghosh, A., Mitsis, G. D. & Boudrias, M.-H. Estimating brain age from structural MRI and meg data: Insights from dimensionality reduction techniques. *NeuroImage* **231**, 117822, DOI: 10.1016/j.neuroimage.2021.117822 (2021).
13. Papakostas, G. A., Savio, A., Graña, M. & Kaburlasos, V. G. A lattice computing approach to Alzheimer's disease computer assisted diagnosis based on MRI data. *Neurocomputing* **150**, 37–42 (2015).
14. Moradi, E., Pepe, A., Gaser, C., Huttunen, H. & Tohka, J. Machine learning framework for early MRI-based Alzheimer's conversion prediction in mci subjects. *Neuroimage* **104**, 398–412, DOI: 10.1016/j.neuroimage.2014.10.002 (2015).
15. Mishra, S., Beheshti, I., Khanna, P. & Initiative, A. D. N. A statistical region selection and randomized volumetric features selection framework for early detection of Alzheimer's disease. *Int. J. Imaging Syst. Technol.* **28**, 302–314, DOI: 10.1002/ima.22290 (2018).
16. Saravanakumar, S. & Thangaraj, P. A voxel based morphometry approach for identifying Alzheimer from MRI images. *Clust. Comput.* **22**, 14081–14089, DOI: 10.1007/s10586-018-2236-6 (2019).
17. FreeSurferVersion3 - Free Surfer Wiki.
18. Lama, R., Gwak, J., Park, J. & Lee, S. Diagnosis of Alzheimer's disease based on structural MRI images using a regularized extreme learning machine and PCA features. *J Heal. Eng* DOI: 10.1155/2017/5485080 (2017).
19. Schmitter, D. *et al.* Alzheimer's disease neuroimaging initiative. an evaluation of volume-based morphometry for prediction of mild cognitive impairment and Alzheimer's disease. *Neuroimage Clin* **8**, 7–17, DOI: 10.1016/j.nicl.2014.11.001 (2014).
20. Gray, K. *et al.* Multi-region analysis of longitudinal FDG-PET for the classification of Alzheimer's disease. *NeuroInage* **60**, 221–229 (2012).
21. Gorriz, J., Segovia, F., Ramírez, J., Lassl, A. & Salas-Gonzalez, D. GMM based SPECT image classification for the diagnosis of Alzheimer's disease. *Appl. Soft Comput.* **1119575757**, 2313–2325, DOI: 10.1016/j.asoc.2010.08.012 (2011).
22. Aguilar, C. *et al.* Different multivariate techniques for automated classification of MRI data in Alzheimer's disease and mild cognitive impairment. *Psychiatry Res. Neuroimaging* **212**, 89–98 (2013).

23. Ebrahimighahnavieh, M. A., Luo, S. & Chiong, R. Deep learning to detect Alzheimer's disease from neuroimaging: A systematic literature review. *Comput. methods programs biomedicine* **187**, 105242, DOI: 10.1016/j.cmpb.2019.105242 (2020).

24. Coupé, P., Catheline, G., Lanuza, E., Manjón, J. V. & Initiative, A. D. N. Towards a unified analysis of brain maturation and aging across the entire lifespan: A mri analysis. *Hum. brain mapping* **38**, 5501–5518, DOI: 10.1002/hbm.23743 (2017).

25. Vinke, E. J. *et al.* Trajectories of imaging markers in brain aging: the Rotterdam Study. *Neurobiol. Aging* **71**, 32–40, DOI: 10.1016/j.neurobiolaging.2018.07.001 (2018).

26. Potvin, O., Dieumegarde, L., Duchesne, S., Initiative, A. D. N. *et al.* NOMIS: Quantifying morphometric deviation from normality over the lifetime in the adult human brain. *bioRxiv* DOI: 10.1101/2021.01.25.428063 (2021).

27. McInnes, L., Healy, J. & Melville, J. UMAP: Uniform Manifold Approximation and Projection for dimension reduction. *Prepr. arXiv:1802.03426* DOI: 10.48550/arXiv.1802.03426 (2018).

28. Van der Maaten, L. & Hinton, G. Visualizing data using t-SNE. *J. machine learning research* **9** (2008).

29. Kruger, U., Zhang, J. & Xie, L. Developments and applications of nonlinear principal component analysis–a review. *Princ. manifolds for data visualization dimension reduction* 1–43, DOI: 10.1007/978-3-540-73750-6_1 (2008).

30. Campbell, J. N. *et al.* A molecular census of arcuate hypothalamus and median eminence cell types. *Nat. neuroscience* **20**, 484–496, DOI: 10.1038/nn.4495 (2017).

31. Becht, E. *et al.* Dimensionality reduction for visualizing single-cell data using UMAP. *Nat. biotechnology* **37**, 38–44, DOI: 10.1038/nbt.4314 (2019).

32. ADNI | Alzheimer's Disease Neuroimaging Initiative. http://adni.loni.usc.edu/.

33. Petersen, R. C. *et al.* Alzheimer's Disease Neuroimaging Initiative (ADNI). *Neurology* **74**, 201–209, DOI: 10.1212/WNL.0b013e3181cb3e25 (2010).

34. Jack, C. R. *et al.* The Alzheimer's Disease Neuroimaging Initiative (ADNI): MRI methods. *J. magnetic resonance imaging: JMRI* **27**, 685–691, DOI: 10.1002/jmri.21049 (2008).

35. Klein, A. & Tourville, J. 101 labeled brain images and a consistent human cortical labeling protocol. *Front. Neurosci.* **6**, 171, DOI: 10.3389/fnins.2012.00171 (2012).

36. Fischl, B. *et al.* Whole brain segmentation: automated labeling of neuroanatomical structures in the human brain. *Neuron* **33**, 341–355, DOI: 10.1016/s0896-6273(02)00569-x (2002).

37. Sherif, T. *et al.* CBRAIN: a web-based, distributed computing platform for collaborative neuroimaging research. *Front. Neuroinformatics* **8** (2014).

38. Belathur Suresh, M., Fischl, B., Salat, D. H. & (ADNI), A. D. N. I. Factors influencing accuracy of cortical thickness in the diagnosis of Alzheimer's disease. *Hum. brain mapping* **39**, 1500–1515, DOI: 10.1002/hbm.23922 (2018).

39. Cardinale, F. *et al.* Validation of FreeSurfer-estimated brain cortical thickness: comparison with histologic measurements. *Neuroinformatics* **12**, 535–542, DOI: 10.1007/s12021-014-9229-2 (2014).

40. How UMAP Works — umap 0.5 documentation. https://umap-learn.readthedocs.io/en/latest/how_umap_works.html.

41. sklearn.cluster.KMeans. https://scikit-learn.org/stable/modules/generated/sklearn.cluster.KMeans.html.

42. sklearn.cluster.kmeans_plusplus. https://scikit-learn.org/stable/modules/generated/sklearn.cluster.kmeans_plusplus.html.

43. Corriveau-Lecavalier, N. *et al.* A quadratic function of activation in individuals at risk of alzheimer's disease. *Alzheimer's & Dementia: Diagn. Assess. & Dis. Monit.* **12**, e12139, DOI: 10.1002/dad2.12139 (2020).

44. Marks, S. M., Lockhart, S. N., Baker, S. L. & Jagust, W. J. Tau and $\beta$-amyloid are associated with medial temporal lobe structure, function, and memory encoding in normal aging. *J. Neurosci.* **37**, 3192–3201, DOI: 10.1523/JNEUROSCI.3769-16.2017 (2017).

45. Teunissen, C. E. *et al.* Blood-based biomarkers for Alzheimer's disease: towards clinical implementation. *The Lancet Neurol.* **21**, 66–77, DOI: 10.1016/S1474-4422(21)00361-6 (2022).

46. Giorgio, J. *et al.* Modelling prognostic trajectories of cognitive decline due to Alzheimer's disease. *NeuroImage: Clin.* **26**, 102199, DOI: 10.1016/j.nicl.2020.102199 (2020).

47. Ersoezlue, E. *et al.* Lifelong experiences as a proxy of cognitive reserve moderate the association between connectivity and cognition in alzheimer's disease. *Neurobiol. Aging* DOI: 10.1016/j.neurobiolaging.2022.05.015 (2022).

## Figure Legend

**Figure 1.** Methodological pipeline for the prediction of cognitive outcome. We first generate a low-dimensional representation of morphology from vectors of features describing the thicknesses of different brain regions using UMAP. Next, we linearly transform the UMAP embedding. In this space, we cluster data using a modified k-means algorithm. This allows us to track aging vs. AD progression trajectories between clusters and therefore compare and predict the future course of individuals that remained either cognitively impaired (MCI), that is in a prodromal state of AD, or declined to clinically probable AD.

**Figure 2.** Defining trajectories. An arbitrary embedding with four clusters. The arrows represent the direction in time for each subject. Given an embedding with clusters we can define the longitudinal trajectory of subjects as follow. In this example, subject 1 would have a full trajectory of [0-1-3-3] while subject 2 [2-3-1]. The trajectory of length 1 would be [3] for subject 1 and [1] for subject 2 and the trajectory of length 3 would be [1-3-3] for subject 1 and [2-3-1] again for subject 2. Subject 2 wouldn't have a trajectory of length 4 and subject 1's would be equivalent to its full trajectory.

**Figure 3.** UMAP embeddings of the NOMIS database using four different values of `n_neighbors`. The age (years) of the participants is color coded. The parameter `min_dist` = 0 for all embeddings. Figure 3**a)** has `n_neighbors` = 3, Figure 3**b)** has `n_neighbors` = 20, Figure 3**c)** has `n_neighbors` = 100 and Figure 3**d)** has `n_neighbors` = 1000. Note that axes have been scaled to fit every point in the frame.

**Figure 4.** Choice of embedding. The correlation between the axes t-UMAP0 (in blue) and t-UMAP1 (in red) with the age of NOMIS' subjects. In green is the difference between the blue and the red line, to show the embeddings that maximise t-UMAP0's while minimizing t-UMAP1's correlations with age. The dashed lines show the maximum and minimum value of the green line after `n_neighbors`=20, value at which the variations in correlation are mostly constrained between these minimum and maximum.

**Figure 5.** Transformed UMAP embedding and fitted ADNI data. Linear transformation applied on the UMAP embedding with `n_neighbors` = 20 to align the principal axes with UMAP0 and UMAP1. In **a)**, the NOMIS database (embedding data) with participants' chronological age (years) at scan color-coded using the color scale displayed on the right. In **b)**, participants from the ADNI database were projected in the NOMIS-defined UMAP embedding. Subject's final diagnosis was used to color the points on **b)**. One notices how the older ADNI participants (age at entry > 65 y.o.) preferentially concentrate along the positive t-UMAP0 direction, congruent with its correlation with age in the NOMIS dataset.

**Figure 6.** Clustering of the ADNI embedding with same size *k*-means. Dimensional reduction of the ADNI database using a linearly transformed UMAP model trained on the NOMIS database using `n_neighbors` = 20 and `min_dist` = 0. The four colors represent the clusters made from the positional values, using a variation of the *k*-means algorithm with `n_clusters` = 4. For simplicity's sake, the axes are not displayed since they are the same as Figure 5

**Figure 7.** Individual and average trajectories for MCI-MCI and MCI-AD subjects. UMAP model shown in Figure 6 with individual trajectories for four MCI-MCI subjects (Figure 7a) and four MCI-ADs (Figure 7b). Different dashed lines are used to differentiate between different subjects and the arrows point in the direction of time. Figure 7c) shows the average trajectories for both types of trajectories. In cluster 3, MCI-ADs are represented by a point because the trajectory is too short to be represented by an arrow.

**Figure 8.** Probabilistic atlas. The distribution of the proportion of AD subjects in each trajectory of size 1 to 3, color coded for the population in each trajectory. For the sake of visibility, unpopulated trajectories are not displayed.

**Figure 9.** ROC curves of 5 different clustering of the transformed UMAP embedding (with 3, 4, 5, 6 and 7 clusters). For each clustering, predictions are made using trajectory length of 1, 2 and 3 last time points. The dashed red line represent the diagonal with area under curve (AUC) of 0.5 for reference. The AUC of each ROC curves is displayed in the table at the bottom right of the figure. This value is obtained by averaging the AUC from 2000 resamplings of the train/test subsets and the value following the $\pm$ is the standard deviation of this distribution. Moreover, the ROC curves displayed are obtained by averaging the ROC curves from 2000 resamplings.

## 1 Acknowledgements

This work was supported by the Natural Sciences and Engineering Research Council of Canada (P.D., N.D), and the Sentinelle Nord program of Université Laval, funded by the Canada First Research Excellence Fund (P.D., N.D.). We acknowledge Calcul Québec and the Digital Research Alliance of Canada for their technical support and computing infrastructures.

This study comprises multiple samples of healthy individuals. We wish to thank all principal investigators who collected these datasets and agreed to let them accessible.

Autism Brain Imaging Data Exchange (ABIDE): Primary support for the work by Adriana Di Martino was provided by the NIMH (K23MH087770) and the Leon Levy Foundation. Primary support for the work by Michael P. Milham and the INDI team was provided by gifts from Joseph P. Healy and the Stavros Niarchos Foundation to the Child Mind Institute, as well as by an NIMH award to MPM (R03MH096321). http://fcon_1000.projects.nitrc.org/indi/abide/

Data collection and sharing for this project was funded by the Alzheimer's Disease Neuroimaging Initiative (ADNI) (National Institutes of Health Grant U01 AG024904) and DOD ADNI (Department of Defense award number W81XWH-12-2-0012). ADNI is funded by the National Institute on Aging, the National Institute of Biomedical Imaging and Bioengineering, and through generous contributions from the following: AbbVie, Alzheimer's Association; Alzheimer's Drug Discovery Foundation; Araclon Biotech; BioClinica, Inc.; Biogen; Bristol-Myers Squibb Company; CereSpir, Inc.; Cogstate; Eisai Inc.; Elan Pharmaceuticals, Inc.; Eli Lilly and Company; EuroImmun; F. Hoffmann-La Roche Ltd and its affiliated company Genentech, Inc.; Fujirebio; GE Healthcare; IXICO Ltd.; Janssen Alzheimer Immunotherapy Research & Development, LLC.; Johnson & Johnson Pharmaceutical Research & Development LLC.; Lumosity; Lundbeck; Merck & Co., Inc.; Meso Scale Diagnostics, LLC.; NeuroRx Research; Neurotrack Technologies; Novartis Pharmaceuticals Corporation; Pfizer Inc.; Piramal Imaging; Servier; Takeda Pharmaceutical Company; and Transition Therapeutics. The Canadian Institutes of Health Research is providing funds to support ADNI clinical sites in Canada. Private sector contributions are facilitated by the Foundation for the National Institutes of Health (www.fnih.org). The grantee organization is the Northern California Institute for Research and Education, and the study is coordinated by the Alzheimer's Therapeutic Research Institute at the University of Southern California. ADNI data are disseminated by the Laboratory for Neuro Imaging at the University of Southern California. http://adni.loni.usc.edu/

Australian Imaging Biomarkers and Lifestyle flagship study of ageing (AIBL): Part of the data used in this study was obtained from the Australian Imaging Biomarkers and Lifestyle flagship study of ageing (AIBL) funded by the Commonwealth Scientific and Industrial Research Organisation (CSIRO) which was made available at the ADNI database (www.loni.usc.edu/ADNI). The AIBL researchers contributed data but did not participate in analysis or writing of this report. AIBL researchers are listed at www.aibl.csiro.au

Berlin Mind and Brain (Margulies, Villringer) CoRR sample (BMB). Zuo, X.N., et al. (2014). An open science resource for establishing reliability and reproducibility in functional connectomics. Scientific data, 1, 140049. doi: 10.1038/sdata.2014.49. http://fcon_1000.projects.nitrc.org/indi/CoRR/html/bmb_1.html

Cambridge Centre for Ageing and Neuroscience (CamCAN): CamCAN funding was provided by the UK Biotechnology and Biological Sciences Research Council (grant number BB/H008217/1), together with support from the UK Medical Research Council and University of Cambridge, UK. http://www.mrc-cbu.cam.ac.uk/datasets/camcan/

Center of Biomedical Research Excellence (COBRE): The imaging data and phenotypic information was collected and shared by the Mind Research Network and the University of New Mexico funded by a National Institute of Health COBRE: 1P20RR021938-01A2. http://fcon_1000.projects.nitrc.org/indi/retro/cobre.html

Cleveland Clinic (Cleveland CCF): Funded by the National Multiple Sclerosis Society.
http://fcon_1000.projects.nitrc.org/indi/retro/ClevelandCCF.html

Consortium for the Early Identification of Alzheimer's Disease (CIMA-Q): Part of the data used in this article were obtained from the Consortium pour l'identification précoce de la maladie Alzheimer - Québec (CIMA-Q). As such, the investigators within the CIMA-Q contributed to the design, the implementation, the acquisition of clinical, cognitive, and neuroimaging data and biological samples. A list of the CIMA-Q investigators is available on http://www.cima-q.ca. CIMA-Q was funded in 2013 with a $2,500,000 grant from the Fonds d'Innovation Pfizer - Fond de Recherche Québec – Santé sur la maladie d'Alzheimer et les maladies apparentées.

Dallas Lifespan Brain Study (DLBS): This study is supported by the Center for Vital Longevity, the University of Texas at Dallas, the University of Texas Southwestern Medical Center, the National Institutes of Health and Aging, AVID Radiopharmaceuticals, the Aging Mind Foundation and the Alzheimer's Association.
http://fcon_1000.projects.nitrc.org/indi/retro/dlbs.html

FIND lab sample. Funded by the Dana Foundation; John Douglas French Alzheimer's Foundation; National Institutes of Health (AT005733, HD059205,HD057610, NS073498, NS058899).
http://fcon_1000.projects.nitrc.org/indi/retro/find_stanford.html

Functional Biomedical Informatics Research Network (FBIRN): Provided by the Biomedical Informatics Research Network under the following support: U24-RR021992, by the National Center for Research Resources at the National Institutes of Health, U.S.A. http://www.birncommunity.org/resources/data/

Lifespan Human Connectome Project in Aging (HCP-Aging): HCP-Aging data were obtained from the National Institute of Mental Health (NIMH) Data Archive (NDA). NDA is a collaborative informatics system created by the National Institutes of Health to provide a national resource to support and accelerate research in mental health. Dataset identifier: http://dx.doi.org/10.15154/1520138. This manuscript reflects the views of the authors and may not reflect the opinions or views of the NIH or of the Submitters submitting original data to NDA. http://nda.nih.gov

International Consortium for Brain Mapping (ICBM). The ICBM (Principal Investigator: John Mazziotta, MD, PhD) was funded was provided by the National Institute of Biomedical Imaging and BioEngineering. ICBM is the result of efforts of co-investigators from UCLA, Montreal Neurologic Institute, University of Texas at San Antonio, and the Institute of Medicine, Juelich/Heinrich Heine University - Germany." https://ida.loni.usc.edu/login.jsp?project=ICBM

Information eXtraction from Images (IXI): Data collected as part of the project EPSRC GR/S21533/02 -
http://brain-development.org/ixi-dataset/

F.M. Kirby Research Center neuroimaging reproducibility data (KIRBY-21). Landman, B.A. et al. "Multi-Parametric Neuroimaging Reproducibility: A 3T Resource Study", NeuroImage. (2010) NIHMS/PMC:252138 doi:10.1016/j.neuroimage.2010.11.047
https://www.nitrc.org/projects/multimodal

Minimal Interval Resonance Imaging in Alzheimer's Disease (MIRIAD): The MIRIAD investigators did not participate in analysis or writing of this report. The MIRIAD dataset is made available through the support of the UK Alzheimer's Society (RF116). The original data collection was funded through an unrestricted educational grant from GlaxoSmithKline (6GKC).
http://miriad.drc.ion.ucl.ac.uk

National Alzheimer's Coordinating Center (NACC): The NACC database is funded by NIA/NIH Grant U01 AG016976. NACC data are contributed by the NIA-funded ADCs: P30 AG019610 (PI Eric Reiman, MD), P30 AG013846 (PI Neil Kowall, MD), P30 AG062428-01 (PI James Leverenz, MD) P50 AG008702 (PI Scott Small, MD), P50 AG025688 (PI Allan Levey, MD, PhD), P50 AG047266 (PI Todd Golde, MD, PhD), P30 AG010133 (PI Andrew Saykin, PsyD), P50 AG005146 (PI

Marilyn Albert, PhD), P30 AG062421-01 (PI Bradley Hyman, MD, PhD), P30 AG062422-01 (PI Ronald Petersen, MD, PhD), P50 AG005138 (PI Mary Sano, PhD), P30 AG008051 (PI Thomas Wisniewski, MD), P30 AG013854 (PI Robert Vassar, PhD), P30 AG008017 (PI Jeffrey Kaye, MD), P30 AG010161 (PI David Bennett, MD), P50 AG047366 (PI Victor Henderson, MD, MS), P30 AG010129 (PI Charles DeCarli, MD), P50 AG016573 (PI Frank LaFerla, PhD), P30 AG062429-01(PI James Brewer, MD, PhD), P50 AG023501 (PI Bruce Miller, MD), P30 AG035982 (PI Russell Swerdlow, MD), P30 AG028383 (PI Linda Van Eldik, PhD), P30 AG053760 (PI Henry Paulson, MD, PhD), P30 AG010124 (PI John Trojanowski, MD, PhD), P50 AG005133 (PI Oscar Lopez, MD), P50 AG005142 (PI Helena Chui, MD), P30 AG012300 (PI Roger Rosenberg, MD), P30 AG049638 (PI Suzanne Craft, PhD), P50 AG005136 (PI Thomas Grabowski, MD), P30 AG062715-01 (PI Sanjay Asthana, MD, FRCP), P50 AG005681 (PI John Morris, MD), P50 AG047270 (PI Stephen Strittmatter, MD, PhD). https://www.alz.washington.edu/

National Database for Autism Research (NDAR): Data were obtained from the National Institute of Mental Health (NIMH) Data Archive (NDA). NDA is a collaborative informatics system created by the National Institutes of Health to provide a national resource to support and accelerate research in mental health. Dataset identifier: http://dx.doi.org/10.15154/1520138. This manuscript reflects the views of the authors and may not reflect the opinions or views of the NIH or of the Submitters submitting original data to NDA. http://nda.nih.gov

Nathan Kline Institute Rockland (NKI-R) sample (NKI-RS) and Enhanced Sample (NKI-RES): Principal support for the NKI-RES project is provided by the NIMH BRAINS R01MH094639-01. Funding for key personnel also provided in part by the New York State Office of Mental Health and Research Foundation for Mental Hygiene. Funding for the decompression and augmentation of administrative and phenotypic protocols provided by a grant from the Child Mind Institute (1FDN2012-1). Additional personnel support provided by the Center for the Developing Brain at the Child Mind Institute, as well as NIMH R01MH081218, R01MH083246, and R21MH084126. Project support also provided by the NKI Center for Advanced Brain Imaging (CABI), the Brain Research Foundation, the Stavros Niarchos Foundation and the NIH P50 MH086385-S1 (NKI-RS ). http://fcon_1000.projects.nitrc.org/indi/pro/nki.html http://fcon_1000.projects.nitrc.org/indi/enhanced/

Open access series of imaging studies (OASIS): The OASIS project was funded by grants P50 AG05681, P01 AG03991, R01 AG021910, P50 MH071616, U24 RR021382, and R01 MH56584. http://www.oasis-brains.org/

POWER: This database was supported by NIH R21NS061144 R01NS32979 R01HD057076 U54MH091657 K23DC006638 P50 MH71616 P60 DK020579-31 , McDonnell Foundation Collaborative Action Award, NSF IGERT DGE-0548890, Simon's Foundation Autism Research Initiative grant, Burroughs Wellcome Fund, Charles A. Dana Foundation, Brooks Family Fund, Tourette Syndrome Association, Barnes-Jewish Hospital Foundation, McDonnell Center for Systems Neuroscience, Alvin J. Siteman Cancer Center, American Hearing Research Foundation grant, Diabetes Research and Training Center at Washington University grant. http://fcon_1000.projects.nitrc.org/indi/retro/Power2012.html

Parkinson's Progression Markers Initiative (PPMI): PPMI – a public-private partnership – is funded by the Michael J. Fox Foundation for Parkinson's Research and funding partners, including Abbvie, Allergan, Amathus, Avid Radiopharmaceuticals, Biogen Idec, BioLegend, Bristol-Myers, Celgene, Cenali, Covance, GE Healthcare, Genentech, GlaxoSmithKline, Glolub Capital, Handl Therapeutics, Insitro, Janssen Neuroscience, Eli Lilly and Company, Lundbeck, Merck, Meso Scale Discovery, Neurocrine, Pfizer, Piramal, Prevail, Roche, Sanofi Genzyme, Servier, Takeda, Teva, UCB, Verily, and Voyager Therapeutics. See http://www.ppmi-info.org for further details.

Southwest University Adult Lifespan Dataset (SALD): SALD was supported by the National Natural Science Foundation of China (31470981; 31571137; 31500885), National Outstanding young people plan, the Program for the Top Young Talents by Chongqing, the Fundamental Research Funds for the Central Universities (SWU1509383,SWU1509451,SWU1609177), Natural Science Foundation of Chongqing (cstc2015jcyjA10106), Fok Ying Tung Education Foundation (151023) , General Financial Grant from the China Postdoctoral Science Foundation (2015M572423, 2015M580767), Special Funds from the Chongqing Postdoctoral Science Foundation (Xm2015037, Xm2016044), Key research for Humanities and social sciences of Ministry of Education (14JJD880009). http://fcon_1000.projects.nitrc.org/indi/retro/sald.html

University of Wisconsin, Madison (Birn, Prabhakaran, Meyerand) CoRR sample (UWM): Zuo, X.N., et al. (2014). An open science resource for establishing reliability and reproducibility in functional connectomics. Scientific data, 1, 140049. doi: 10.1038/sdata.2014.49 http://fcon_1000.projects.nitrc.org/indi/CoRR/html/uwm_1.html

Wayne State EF Dataset: This dataset was supported by National Institute on Aging grants R01-AG011230, R37-AG011230, R03-AG024630 to Naftali Raz, Ph.D. http://fcon_1000.projects.nitrc.org/indi/retro/wayne_EF.html

Yale Low-Resolution Controls Dataset: Scheinost D, Tokoglu F, Shen X, Finn ES, Noble S, Papademetris X, Constable RT. Fluctuations in Global Brain Activity Are Associated With Changes in Whole-Brain Connectivity of Functional Networks. IEEE Trans Biomed Eng. 2016 Dec;63(12):2540-2549. Epub 2016 Aug 16. http://fcon_1000.projects.nitrc.org/indi/retro/yale_lowres.html

## Author contributions statement

N.D., P.D, and S.D. designed the project. O.P, R.L-C., and S.D. collected and prepared the data. R.L-C. wrote the codes and conducted the numerical experiments. All authors analyzed the results. R.L-C. wrote the main manuscript text while N.D., P.D, and S.D. revised, verified the results, and improved the writing of the manuscript.

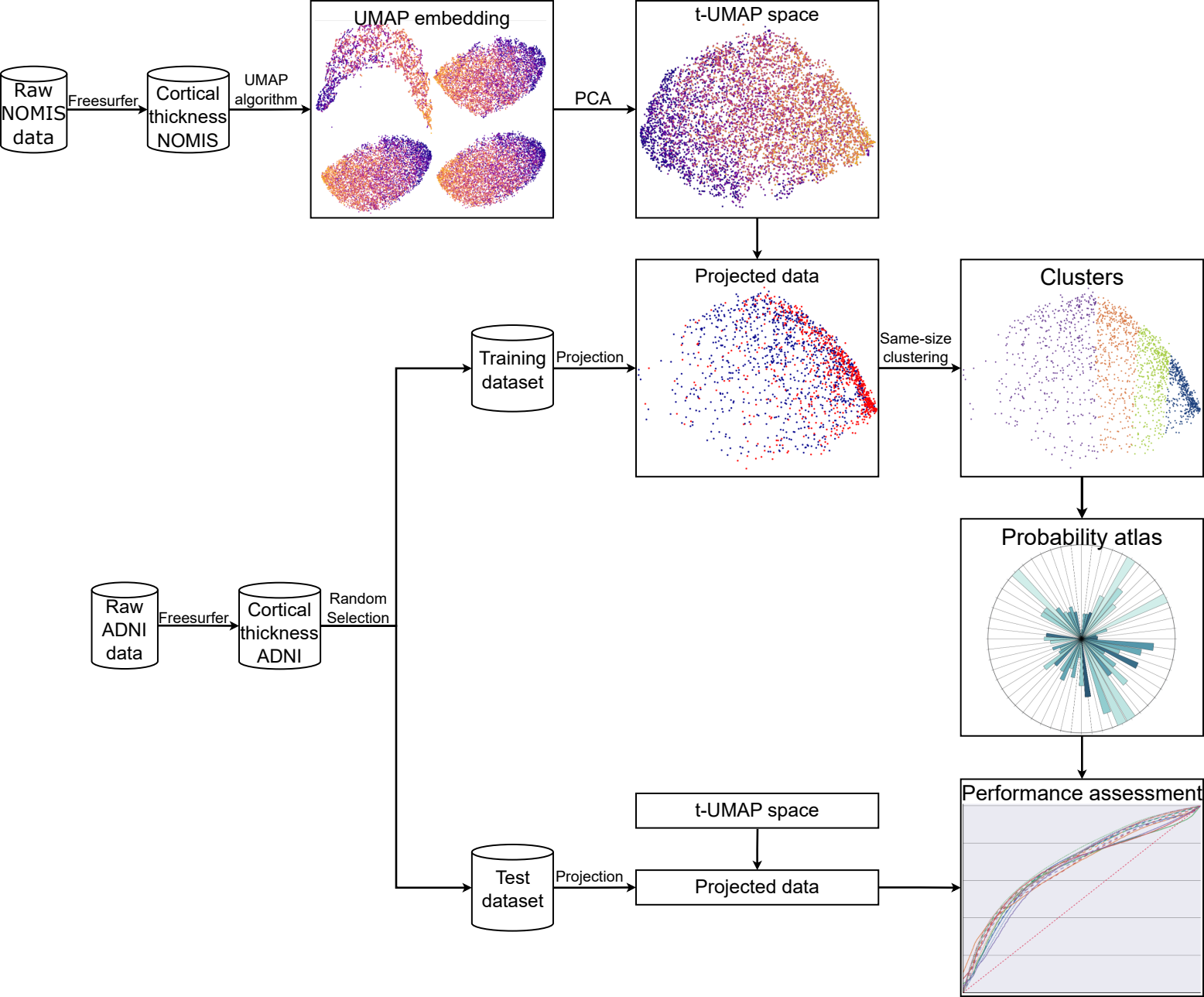
Raw NOMIS data
Freesurfer
Cortical thickness NOMIS
UMAP algorithm
UMAP embedding
PCA
t-UMAP space
Projected data
Same-size clustering
Clusters
Training dataset
Projection
Probability atlas
Raw ADNI data
Freesurfer
Cortical thickness ADNI
Random Selection
Performance assessment
t-UMAP space
Test dataset
Projection
Projected data

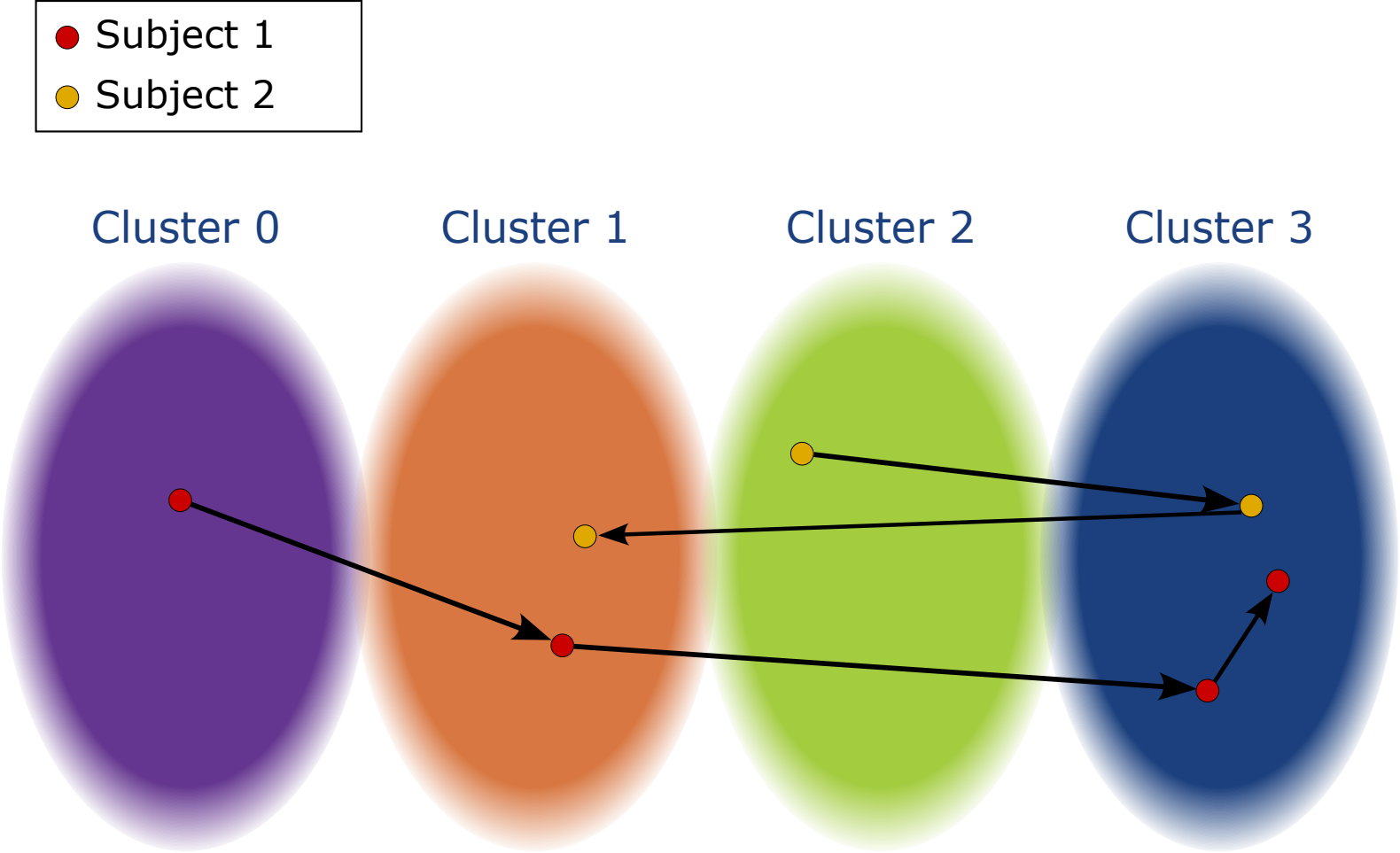
Subject 1
Subject 2
Cluster 0
Cluster 1
Cluster 2
Cluster 3

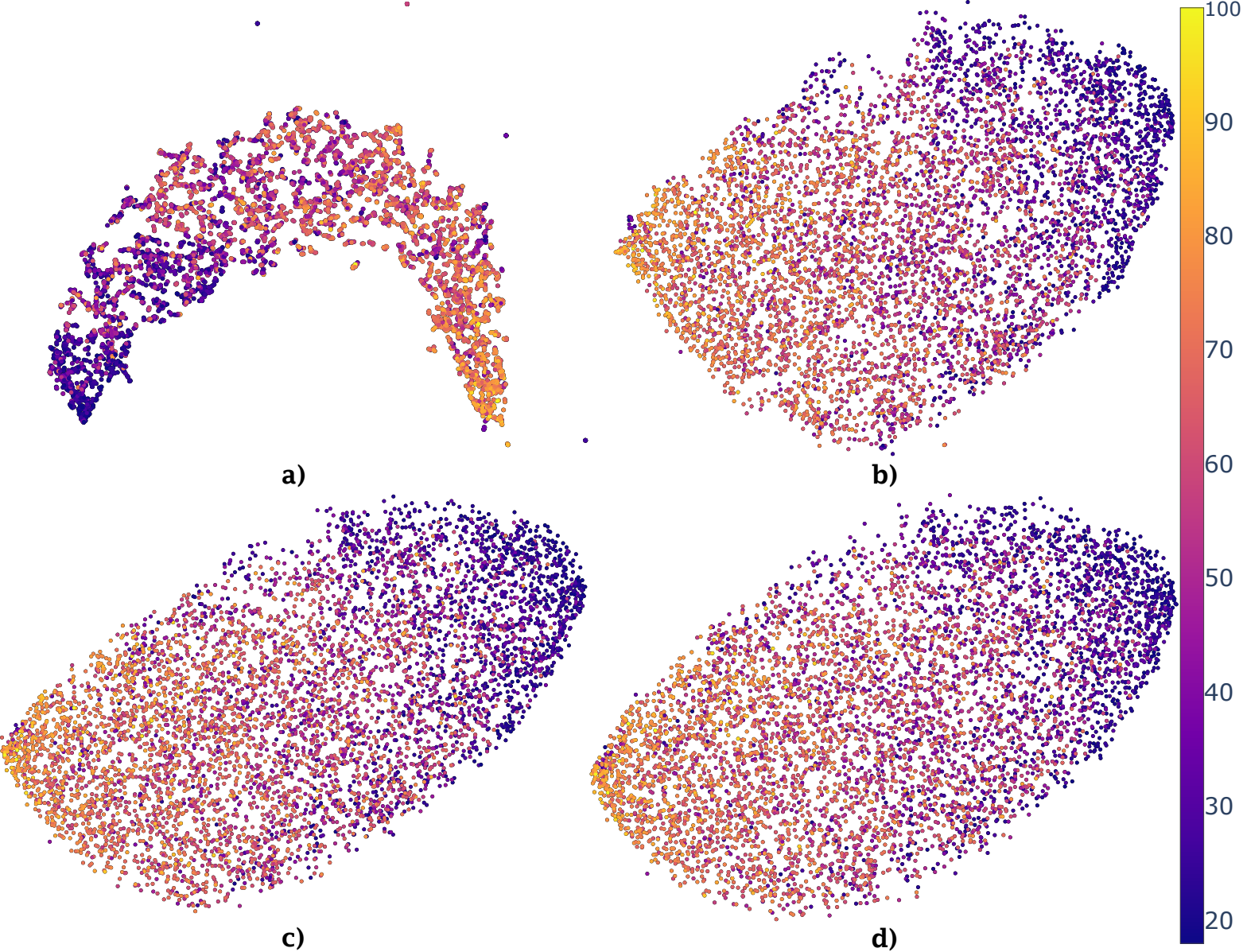
a)
b)
c)
d)
100
90
80
70
60
50
40
30
20

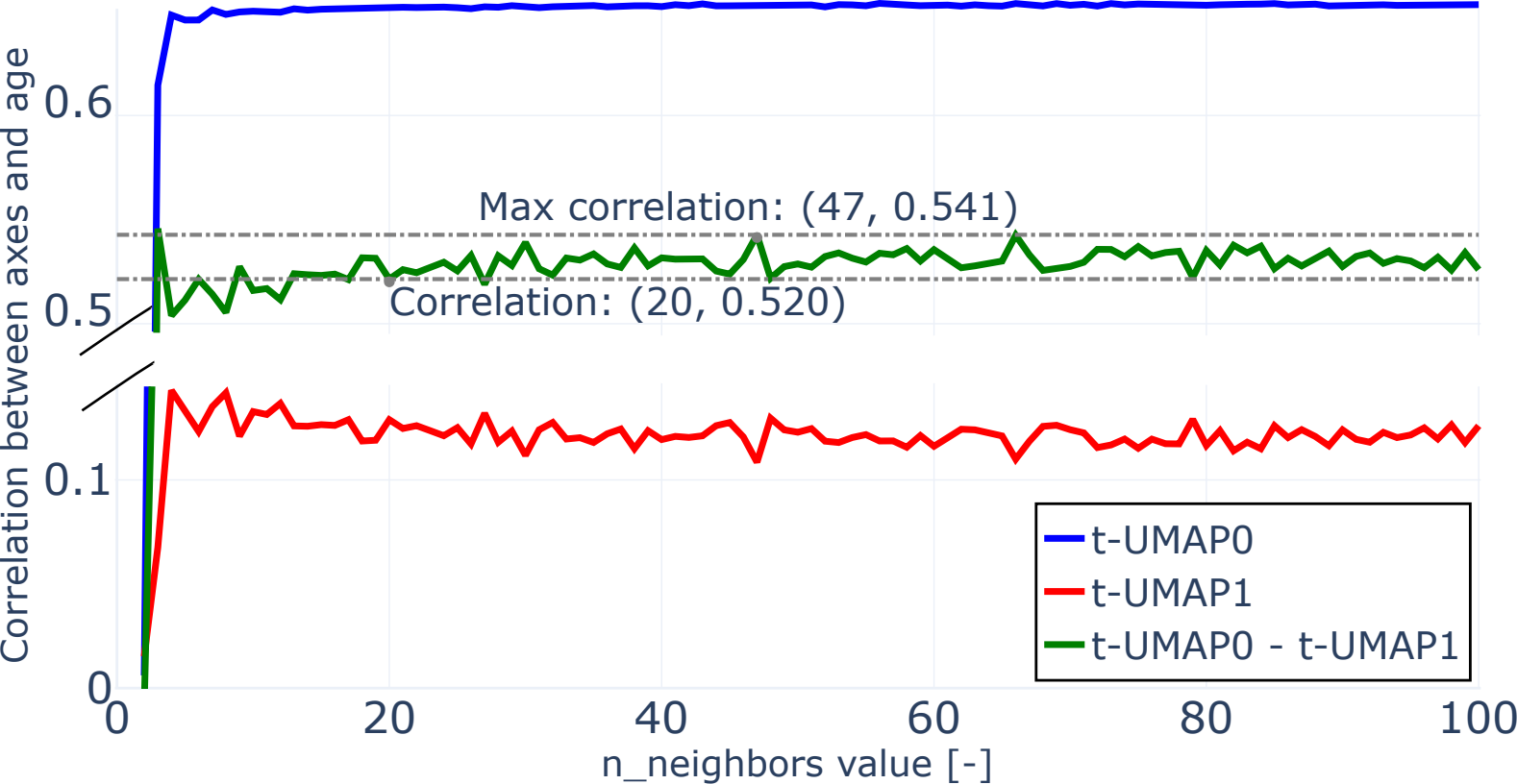
Correlation between axes and age
0.6
0.5
0.1
0
Max correlation: (47, 0.541)
Correlation: (20, 0.520)
t-UMAP0
t-UMAP1
t-UMAP0 - t-UMAP1
0
20
40
60
80
100
n_neighbors value [-]

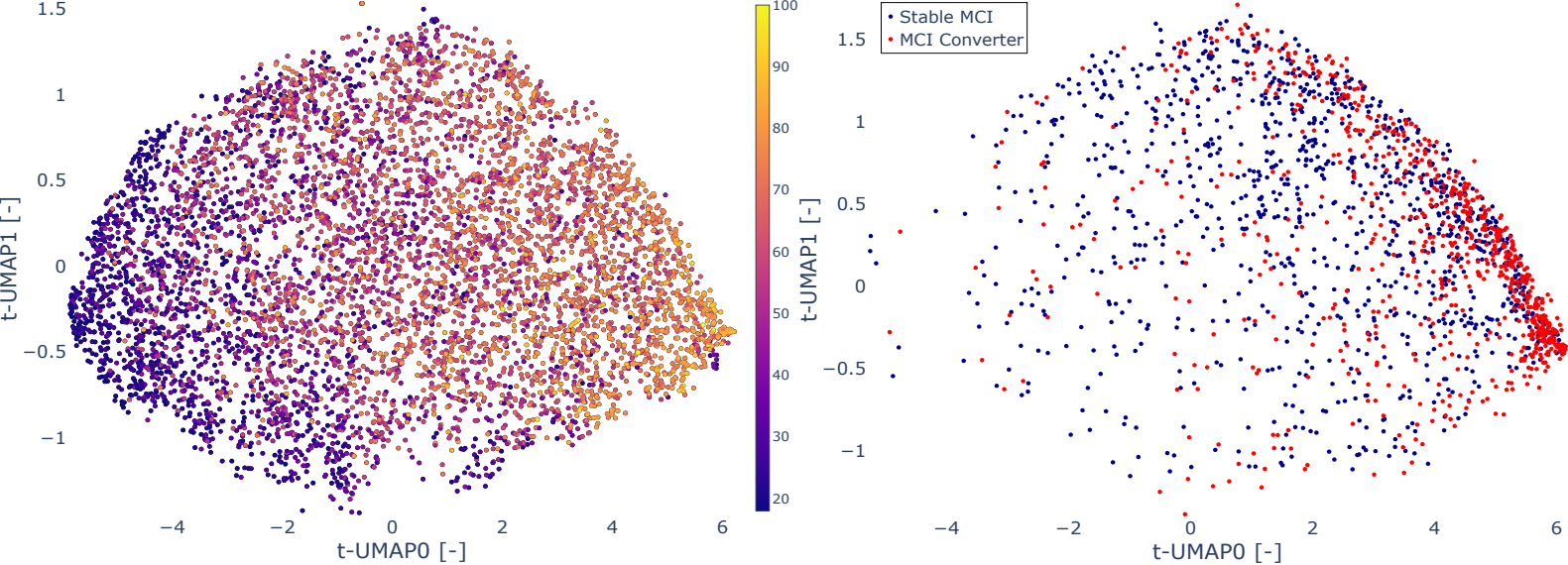


**a)** NOMIS embedding, color coded for age **b)** ADNI data color coded for the final diagnosis

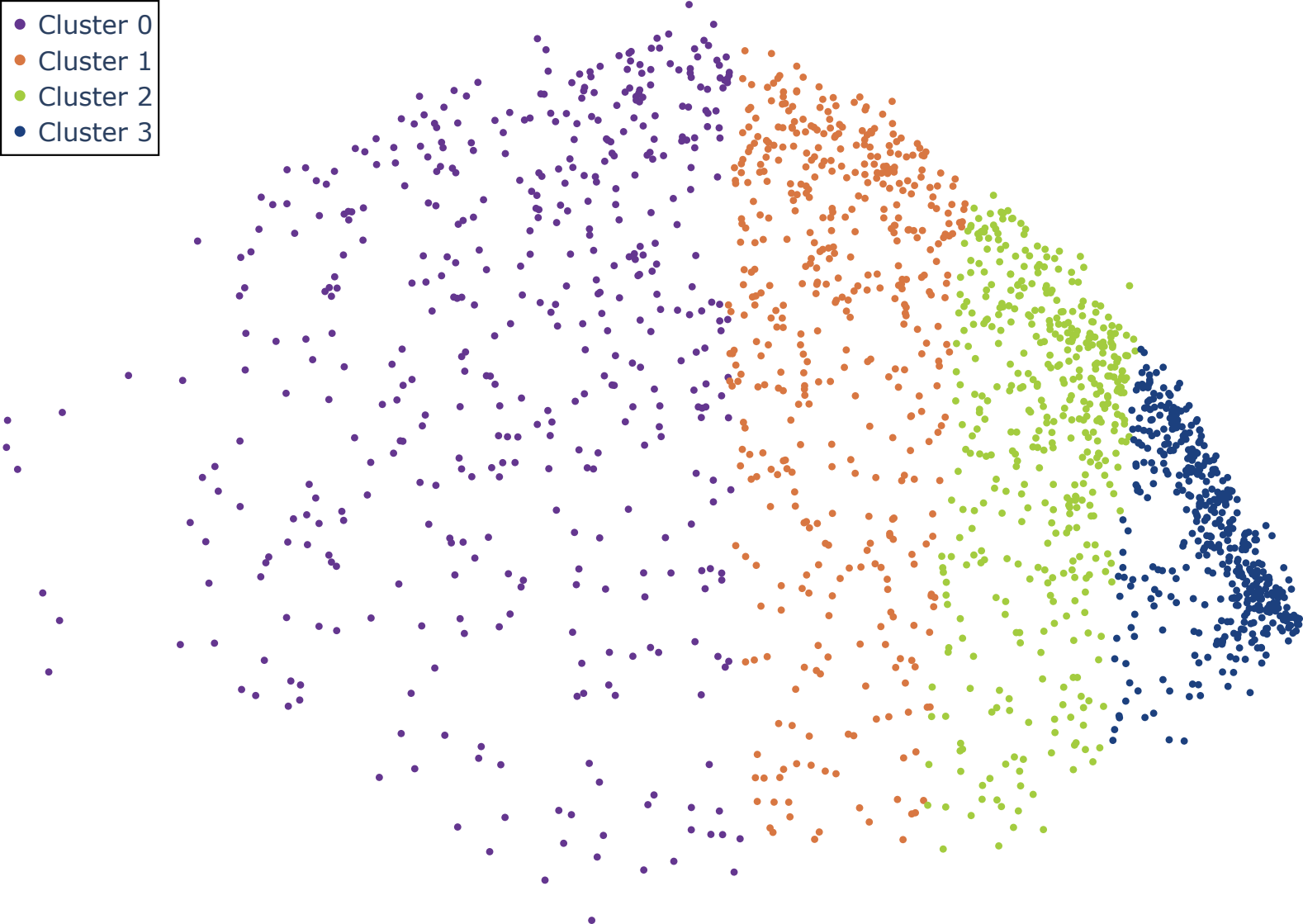
Cluster 0
Cluster 1
Cluster 2
Cluster 3

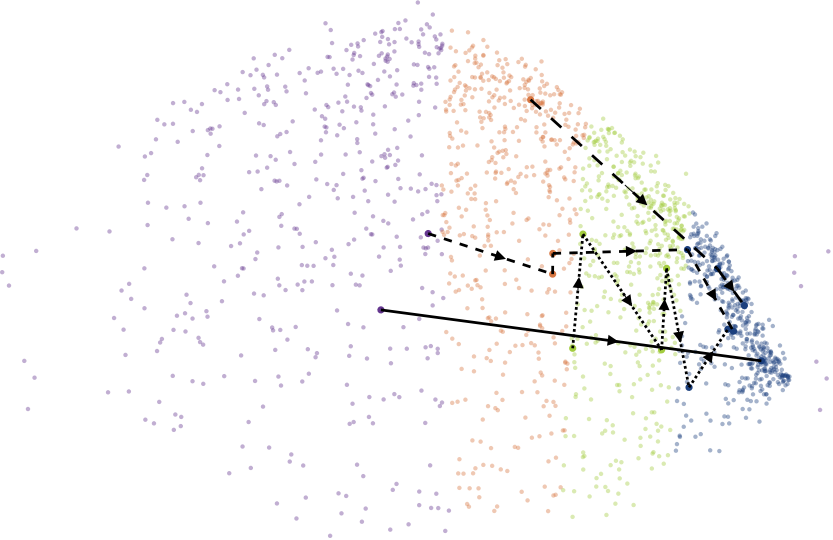

**a)** Stable trajectory examples

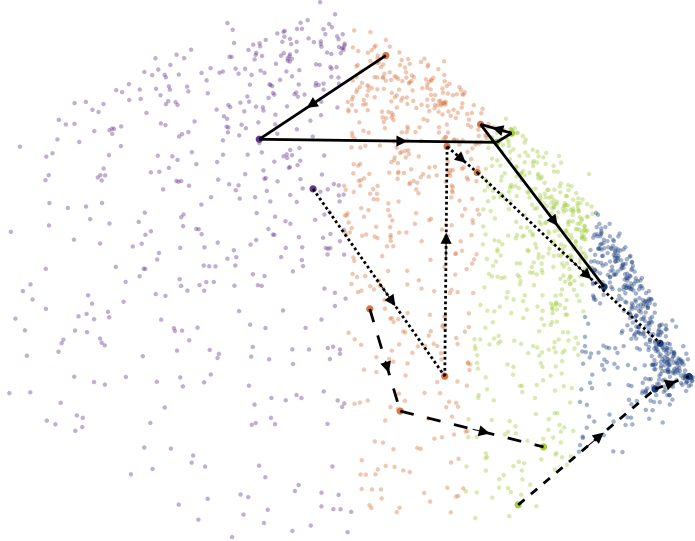

**b)** Converter trajectory examples

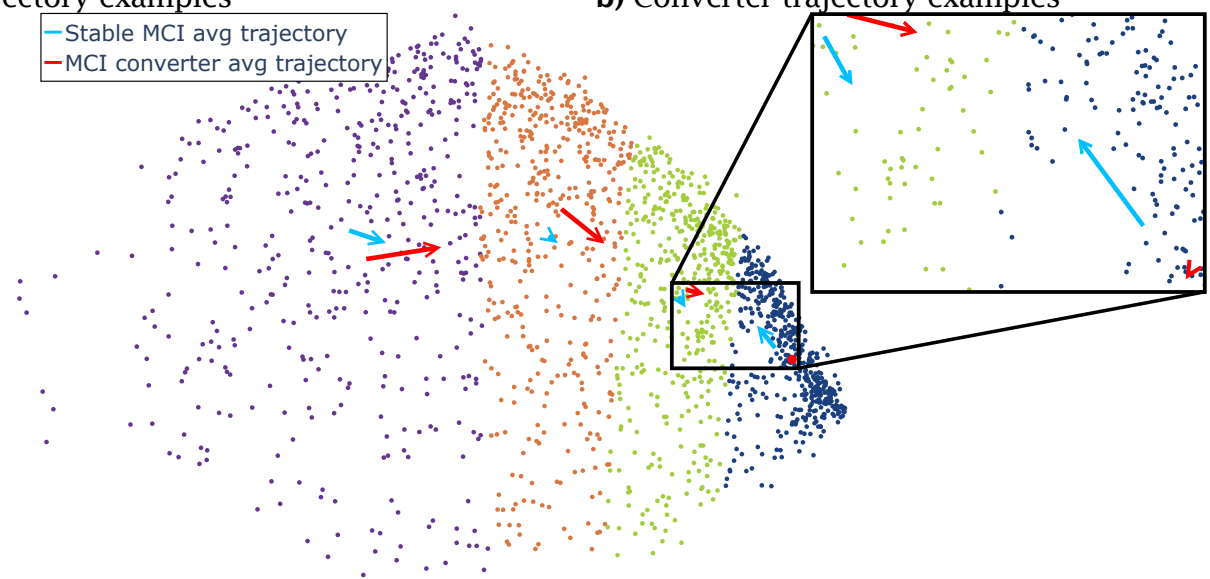


**c)** Average trajectories in each cluster for MCI converter (red) and MCI stable (blue)

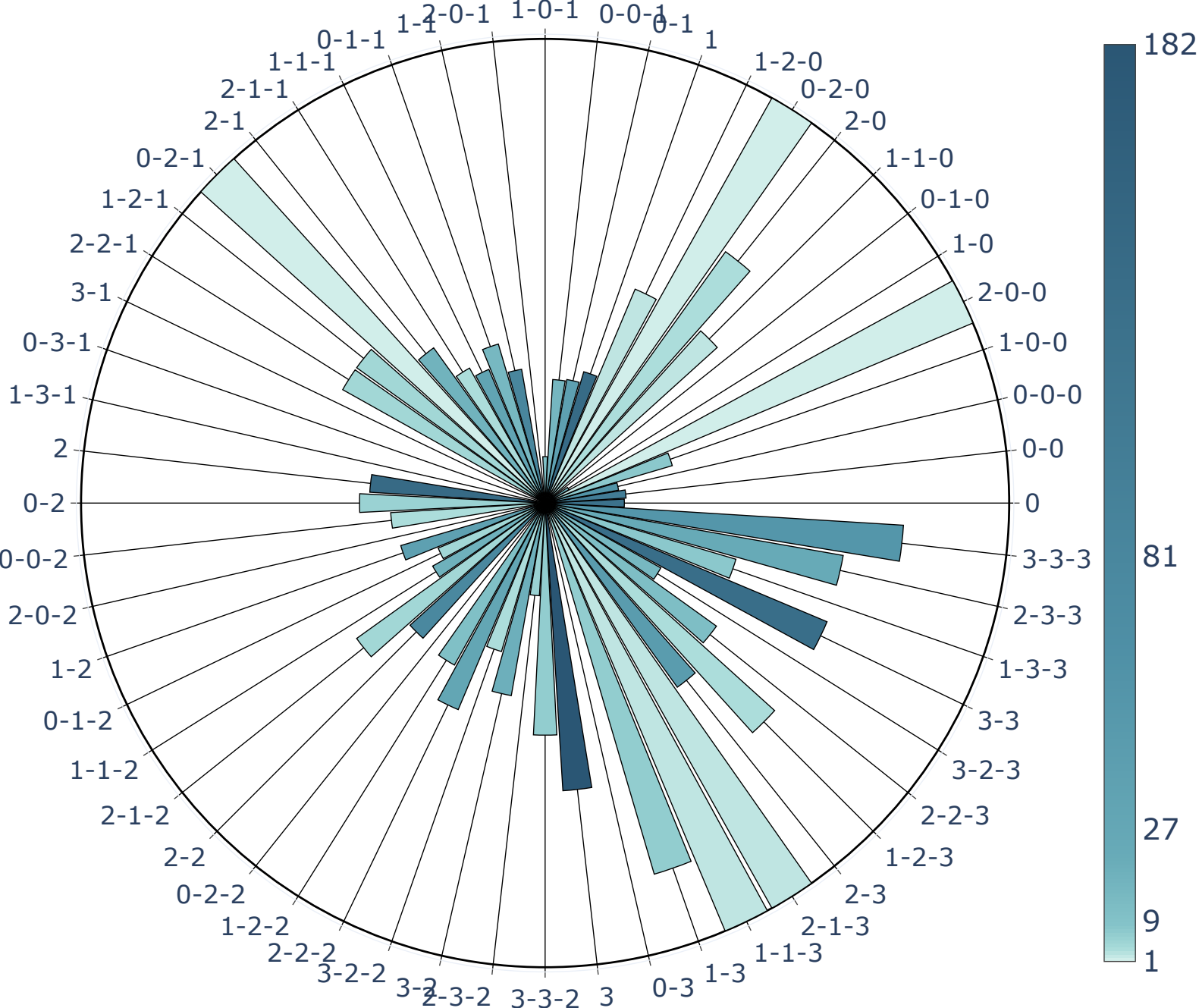
1-0-1
0-0-1
0-1
1
1-2-0
0-2-0
2-0
1-1-0
0-1-0
1-0
2-0-0
1-0-0
0-0-0
0-0
0
3-3-3
2-3-3
1-3-3
3-3
3-2-3
2-2-3
1-2-3
2-3
2-1-3
1-1-3
1-3
0-3
3
3-3-2
2-3-2
3-2
3-2-2
2-2-2
1-2-2
0-2-2
2-2
2-1-2
1-1-2
0-1-2
1-2
2-0-2
0-0-2
2
1-3-1
0-3-1
3-1
2-2-1
1-2-1
0-2-1
2-1
2-1-1
1-1-1
0-1-1
1-1
2-0-1
182
81
27
9
1

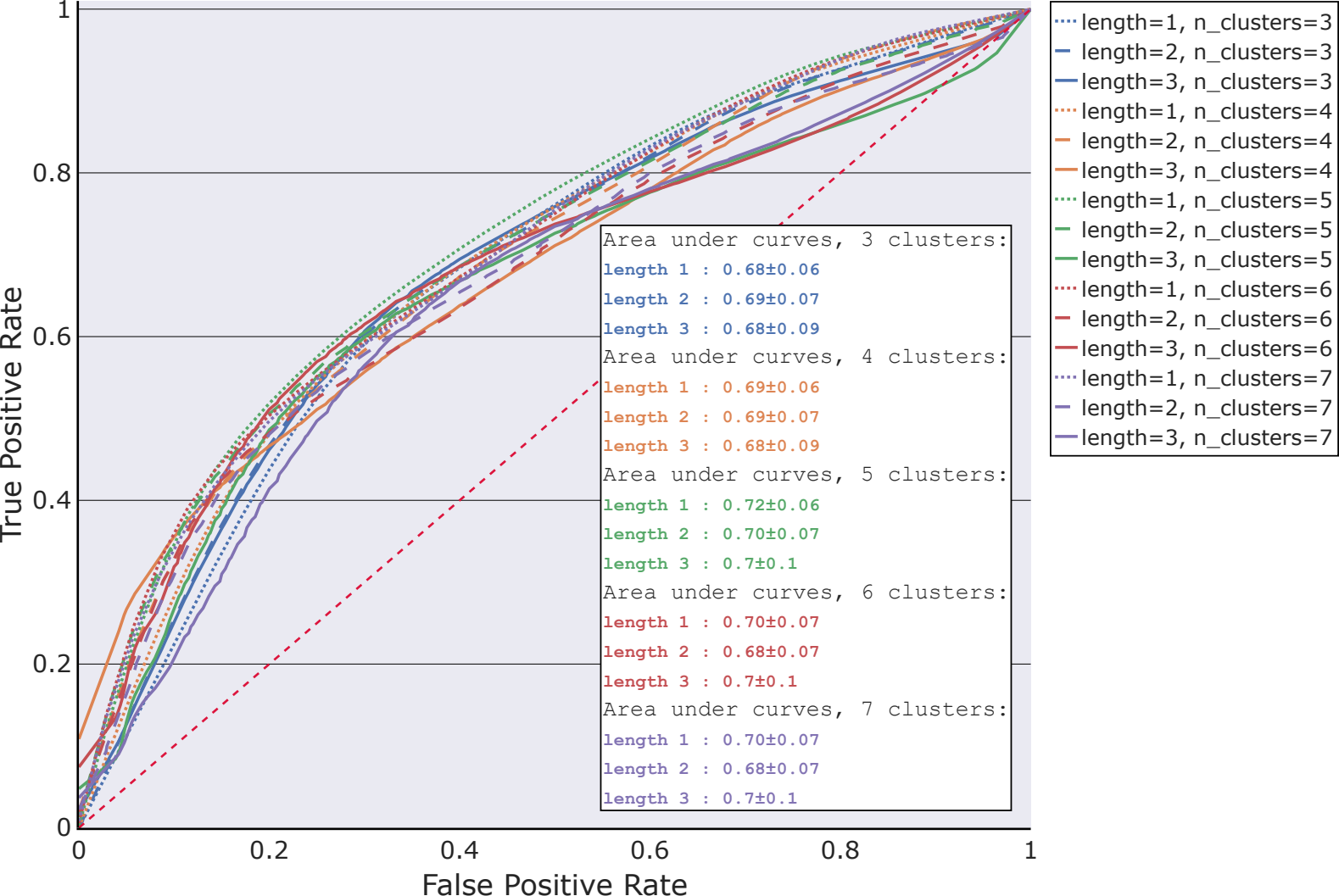
True Positive Rate
False Positive Rate
0
0.2
0.4
0.6
0.8
1
length=1, n_clusters=3
length=2, n_clusters=3
length=3, n_clusters=3
length=1, n_clusters=4
length=2, n_clusters=4
length=3, n_clusters=4
length=1, n_clusters=5
length=2, n_clusters=5
length=3, n_clusters=5
length=1, n_clusters=6
length=2, n_clusters=6
length=3, n_clusters=6
length=1, n_clusters=7
length=2, n_clusters=7
length=3, n_clusters=7
Area under curves, 3 clusters:
length 1 : 0.68±0.06
length 2 : 0.69±0.07
length 3 : 0.68±0.09
Area under curves, 4 clusters:
length 1 : 0.69±0.06
length 2 : 0.69±0.07
length 3 : 0.68±0.09
Area under curves, 5 clusters:
length 1 : 0.72±0.06
length 2 : 0.70±0.07
length 3 : 0.7±0.1
Area under curves, 6 clusters:
length 1 : 0.70±0.07
length 2 : 0.68±0.07
length 3 : 0.7±0.1
Area under curves, 7 clusters:
length 1 : 0.70±0.07
length 2 : 0.68±0.07
length 3 : 0.7±0.1